

A Spectrally Resolved Thermal Model for a PV + PCM System

C.K. de Mooij

Delft University of Technology

A Spectrally Resolved Thermal Model for a PV + PCM System

by

C.K. de Mooij

to obtain the degree of Master of Science

at the Delft University of Technology,

to be defended publicly on Friday November 27th, 2020 at 10:00 AM.

Student number: 4285018
Project duration: September 26, 2019 – November 27, 2020
Thesis committee: Dr. ir. O. Isabella, TU Delft, supervisor
Dr. ir. R. Santbergen, TU Delft
Dr. ir. C. Infante Ferreira, TU Delft
Dr. ir. H. Ziar, TU Delft, daily supervisor
Ir. J. C. Ortiz Lizcano, TU Delft, daily supervisor

An electronic version of this thesis is available at <http://repository.tudelft.nl/>.

Abstract

As the world is trying to rely less on fossil fuels for electrical energy. To do this, the alternatives should be as efficient and durable as possible. The alternative that has been growing the fastest in recent years is *solar energy*. Apart from its growth in the market share, the efficiency of photovoltaic (PV) cells has also steadily grown. Recently, this trend has started to stagnate, since most avenues of efficiency improvement have been exhausted. However, the possibilities of thermal management (i.e. cooling) of PV cells are relatively unexplored. An increase in cell temperature causes a decrease in efficiency, in other words, less sunlight is converted into electrical energy. Moreover, high operating temperatures cause damage in solar cells, reducing their lifetime by months (or even years). One promising technology that can keep cell temperatures low is the Phase Change Material (PCM) based heat sink. A PCM takes a lot of energy to melt and during phase change it remains at a stable temperature. PV + PCM systems have shown to be able to increase cell efficiency by up to 8%. In order to get a better grip on the workings and the potential of PCMs as a heat sink for PV cells, this work presents an implicit, transient, spectrally resolved, MATLAB-based model that can simulate module temperature and phase change within the PCM. The model uses SMARTS in combination with irradiance data to create spectral irradiance data. Using this spectral data together with GenPro4 provides the amount of energy absorbed by each layer of the PV cell. The PV part of the model is validated for a summer week in the Netherlands, with a Mean Absolute Error (MAE) of 1.83 and a Mean Bias Error (MBE) of 0.56. For a winter week in January the MAE was 1.76 and the MBE -1.44. When simulating only a PV module (so no PV + PCM system), the model can simulate 45 hours of data per hour, with one minute time step. When validating the PV + PCM model for the same weeks, the MAE was 2.96 and the MBE 1.91 for the summer week and a MAE of 1.37 and MBE of -1.15 for the winter week. When simulating a PV + PCM system the simulation time drops to 18 hours of simulated data per hour, due to a larger mesh and the requirement of several iterations in the PCM model. With this model a wide range of PV + PCM systems (e.g. with different thicknesses and melting temperatures) can be simulated for any location, provided that there is access to the following weather data: temperature, wind speed and irradiance.

Acknowledgements

First of all I'd like to thank my two daily supervisors, Ir. Juan Camilo Ortiz Lizcano and Dr.ir. Hesan Ziar. Always responding to questions blazingly fast (even late at night), combined with unwavering support made Juan Camilo an excellent supervisor, I will cherish your supervision for a long time. Hesan, you are a soft-spoken man, but once you give feedback it is sharp and to the point. Next, I'd like to thank Prof. dr.ir. Olindo Isabella for granting me a place to graduate at his department and for being my chair. Speaking of my thesis committee I'd like to thank Dr.ir. Rudi Santbergen and Dr.ir. Carlos Infante Ferreira for being part of it. I'd also like to thank Rudi separately for helping with GenPro4, what an amazing piece of software!

I also would like to thank my family for believing in me, when I don't necessarily do. With special thanks, of course, to my girlfriend Kati, whose positive outlook on life has made everything so much less stressful. I'd like to thank Andreas and Michaël for being great house mates, nobody had ever thought we'd live in the same house until we graduated. Finally I'd like to thank Dispuut Redux for being the backbone of my student life.

*C.K. de Mooij
Delft, November 2020*

Contents

List of Figures	xi
List of Tables	xiii
1 Introduction	1
1.1 Improving the energy yield of solar energy	1
1.2 Keeping the operating temperatures low	2
1.2.1 The role of Phase Change Materials	2
1.3 Aim of this thesis	3
1.4 Structure of this thesis	3
2 Theory and background	5
2.1 Electrical energy from the sun	5
2.1.1 The solar spectrum	5
2.1.2 Reflection, absorption and transmission of light	6
2.1.3 From absorbed light to electrical energy	6
2.2 Heat generation in a solar cell	7
2.2.1 From absorbed light to heat	7
2.2.2 Effect of temperature on cell efficiency	7
2.3 Heat transfer and cooling methods	8
2.3.1 Conduction	8
2.3.2 Convection	9
2.3.3 Radiation	9
2.3.4 Cooling methods	9
2.4 Phase Change Materials as cooling method	10
3 A one-dimensional spectrally resolved thermal model	13
3.1 Nodal Network and variable mesh algorithm	13
3.2 Energy Balance Method	15

3.3	Internal heating using SMARTS and GenPro4	17
3.4	Input overview	18
3.5	PCM model	18
3.6	Solving methodology	19
4	Validation	21
4.1	PCM model validation	21
4.2	Note on error calculations	22
4.3	Validation of the spectral input (SMARTS)	22
4.4	Validating thermal model without PCM	24
4.4.1	System location and geometry	24
4.4.2	Nodal network and time steps	24
4.4.3	Model performance in summer	25
4.4.4	Model performance in winter	26
4.5	PV + PCM validation	28
4.5.1	Physical parameters and geometry	28
4.5.2	PV+PCM model performance during summer	28
4.5.3	PV+PCM model performance during winter	29
4.6	Review of model performance	31
5	Discussion	33
5.1	The effects of wind speed on module temperature	33
5.2	Sensitivity analysis on PCM parameters	35
6	Conclusions and Outlook	39
6.1	Conclusion	39
6.2	Model improvements	40
6.2.1	Improving computational times	40
6.2.2	Adding electrical output	40
6.2.3	Improving SMARTS integration	40
6.2.4	Adding cloudiness dependency to spectral irradiance data	40
6.2.5	Improving physical inputs	40

6.3 Model applications 41

6.3.1 Mapping the global potential of PV + PCM systems 41

6.3.2 Integration with the PV systems modelling toolbox of the PVMD group 41

Bibliography **43**

List of Figures

1.1	The progression of research cell record efficiencies, with the c-Si technologies highlighted [4].	2
2.1	The solar spectrum, both at the top of the atmosphere and at ground level [14].	5
2.2	Schematic representation of the transmission, reflection and refraction of light as it traverses several media [15]. In the case of a PV module, n_1 could be air, n_2 glass and n_3 the solar cell material or its encapsulant.	6
2.3	Schematic representation of the band gap in a: A. Conductor, B. Insulator and C. Semiconductor. For the semiconductor it is shown how when an electron is excited to the conduction band, a "hole" stays behind in the valence band (adapted from [16]). . .	7
2.4	The effect of temperature on the IV curve of a solar cell [18].	8
2.5	Using the latent heat of a PCM, more energy can be stored. In other words, more heat from the solar cell can be absorbed, compared to using a material that does not change phase (indicated by the dotted line) [29].	10
3.1	Schematic example of the relation between the layer thickness d , the spacial increments, Δx , and the amount of nodes in each layer. In this example there are three nodes in each layer, $i = 2$ and $N = 3$	13
3.2	Between to differently sized space increments Δx , the control volume has a different thickness than the usual $d_{cv} = \Delta x$	15
3.3	A flowchart depicting all the calculations and data required for the main solver of the model.	18
4.1	Simulation of the melting process of a PCM.	22
4.2	Spectral data generated by SMARTS compared to spectral measurements. The first column shows results from the 24 th of February 2020, the second of the 7 th of July 2020. The three rows consist of data from sunrise, highest solar point and sunset respectively.	23
4.3	Model output and measured temperatures of a PV module during the first week of September 2019	25
4.4	Absolute difference between the model output and the measured temperature values for a PV module, during first week of September 2019	25
4.5	Difference (prediction - measurement) between the measured and simulated temperatures, during the first week of September 2019, of a PV module installed at the TU delft. The MAE and MBE are also shown.	26
4.6	Model output and measured temperatures of a PV module during the first week of January 26	

4.7	Absolute difference between the model output and the measured temperature values of a PV module, during the first week of January	27
4.8	Difference (prediction - measurement) between the measured and simulated temperatures, during the first week of January 2020, of a PV module installed at the TU delft. The MAE and MBE are also shown.	27
4.9	Model output and measured temperatures of the PV + PCM system in the first week of September	28
4.10	Absolute difference between the model output and the measured values of the PV + PCM system for the first week of September	29
4.11	Difference (prediction - measurement) between the measured and simulated temperatures, during the first week of September 2019, of the PV + PCM system. The MAE and MBE are also shown.	29
4.12	Measured and simulated module temperature of a PV + PCM system, during the first week of January 2020.	30
4.13	Absolute difference between simulated temperatures and measured values for the PV +PCM system, during the first week of January 2020	30
4.14	Difference (simulation - measurement) between simulated temperatures and measured values for the PV + PCM system, during the first week of January 2020. The MAE and MBE are also shown.	30
5.1	Module temperature for January 2 nd 2020 for different wind speeds. The measured ambient temperature is also shown.	33
5.2	Measured wind speed at the TU Delft PV monitoring station on the 2 nd of January	34
5.3	Module temperature for January 2 nd 2020 for different convection heat transfer coefficient calculations. The baseline uses equation 5.1, the higher offset refers to equation 5.2. . . .	34
5.4	Measured and simulated module temperatures for the first week of January 2020. The different h models refer to eq. 5.2 and eq. 5.2	35
5.5	Absolute difference between measurements and the simulated module temperatures shown in figure 5.4.	35
5.6	Difference (prediction - observation) between measurements and the simulated module temperatures shown in figure 5.4. The MAE and MBE refer to the error between the measured temperatures and the simulated temperatures using Test et al.	36
5.7	measured and simulated PV module temperatures for the second day of September 2019. The module temperatures are simulated for different thermal diffusivities (α) and compared with the original simulation (Rubitherm-25)	36
5.8	measured and simulated PV module temperatures for the second day of September 2019. The module temperatures are simulated with a different thickness distribution in the PCM slab.	37

List of Tables

4.1	Materials used for the PV modules at the PV monitoring station of the Delft University of Technology [37].	24
4.2	Material data used for the PCM and its plastic encapsulant.	28

Introduction

In a world of depleting fossil fuel resources and the looming threat of climate change, the sustainable energy industry has been growing quickly. One of the fastest growing industries within the sustainable energy sector has been the photovoltaic (PV) energy industry [1], the technology to harvest electrical energy from sunlight. The PV module (a *solar panel*) is the most well known product of this industry. A PV module is the frame and encapsulation of a PV device (a *solar cell*), the part of the module that converts sunlight in to electrical energy. There are several types of photovoltaic cells on the market, but the crystalline silicon (c-Si) solar cell is the most popular type currently produced (with almost 95% of the market share [2]). This thesis will cover a model to help with the improvement of c-Si solar cell energy yield by using Phase Change Materials as an innovative cooling method.

1.1. Improving the energy yield of solar energy

For commercial and sustainability reasons PV modules should produce as much energy as possible during their lifetime. There are four main fields of research that focuses on maximising this energy yield:

- increasing the efficiency of the solar cell
- increasing the amount of light that reaches the solar cell
- increasing the effective area of a PV module
- increasing the lifetime of a PV module

The efficiency of c-Si solar cells has been steadily increasing since the 1970s, but in the last few years it is starting to get closer to its physical maximum (which is calculated to be 29.43% [3]). As a result the record efficiencies of the most high-end research cells is starting to plateau, as can be seen in figure 1.1. Since these state-of-the-art technologies still have to be implemented into commercial PV modules, their efficiency will keep increasing in the upcoming years, but the point where increasing the efficiency is not profitable any more is in sight.

Maximising the amount of light that reaches the solar cell can be done at several scales. On a larger scale the module can track the sun (either on one or two axes [5]) or concentrate the light onto the module using lenses or mirrors [6]. On module scale, one can use anti-reflective coatings that direct more light to the solar cell[7]. On smaller scales there are many innovative ways to trap light within the solar cell, from adding nano-scale texturing [8] to the layers of the solar cell, to adding nano-particles to the materials themselves [9].

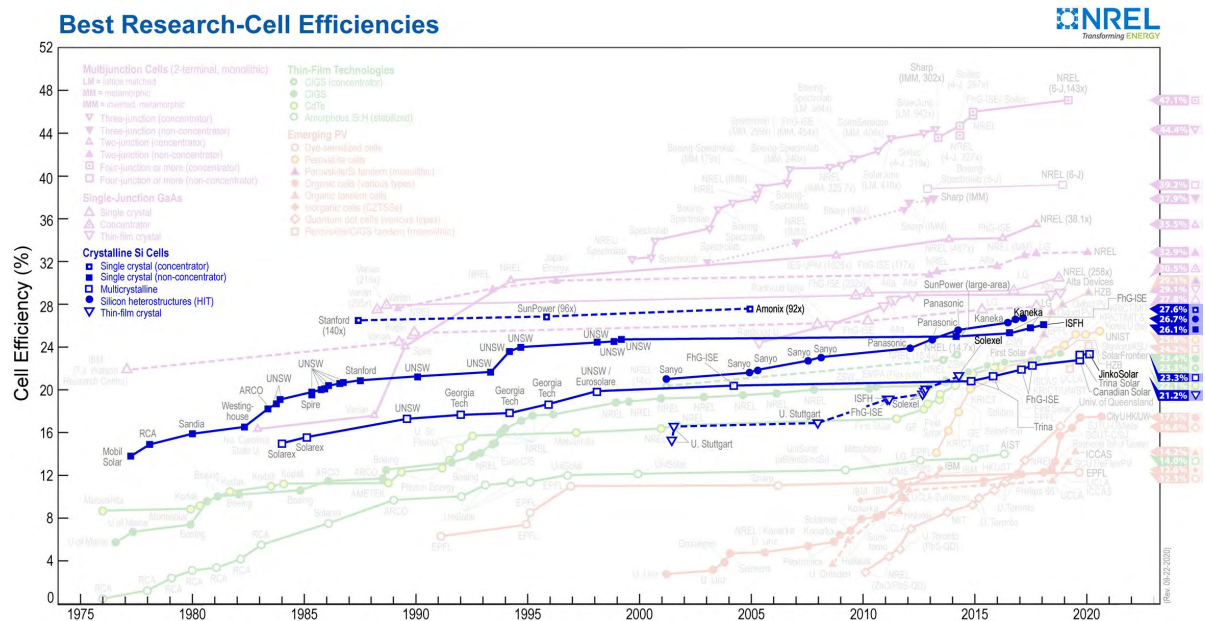


Figure 1.1: The progression of research cell record efficiencies, with the c-Si technologies highlighted [4].

In order to increase the effective area of a solar module, manufacturers have started to make the frames that contain the solar cells slimmer, and with modern solar cell technologies (interdigitated back contacts [10]) it is now possible to get rid of the front surface metallic contacts of a PV cell. However, similar to increasing the efficiency of a solar cell, there is a clear endpoint in sight: a solar cell with an effective area of (almost) 100%.

When the goal is to improve the energy yield of a solar module over the entirety of its lifespan, one can also try to increase the lifetime of the module. To do this, manufacturers can use more durable materials for instance. But one way to increase the lifetime of a PV module, which is also the focus of this thesis, is to keep the operating temperatures of the cell low.

1.2. Keeping the operating temperatures low

Keeping the operating temperatures of a PV cell low, preferably under 43°C [11], drastically increases the lifetime of a PV cell. Moreover, the lower the cell temperature, the higher the cell efficiency. Combining these two factors makes thermal management of PV cells an attractive way to improve the total energy yield of a PV module, chapter 2 will give an overview of cooling methods that are being currently researched or used.

1.2.1. The role of Phase Change Materials

One innovative way of cooling a PV module is the addition of a Phase change Material to the back surface of a PV module, which is the focus of this work. A PCM is a material that takes a substantially large amount of energy to melt or solidify compared to other materials. An example from day-to-day life would be a hot-cold pack. Such a pack, when frozen, stays cold and solid for a very long time. If such a material is placed at the back of a PV module it could act as a heat sink that maintains a stable temperature for as long as its melting. When this fixed temperature is around the critical operating temperature of a PV cell, the PCM can prevent the PV cell from heating up too much.

1.3. Aim of this thesis

A detailed model of a PV + PCM system is required to study the effectiveness of PV + PCM systems under different environmental conditions and at different locations. This thesis strives to present a flexible model, using MATLAB [12], that uses readily available inputs in order to aid future researchers. Flexible meaning that the model should be able to work for many different PV module set-ups. The model should be able to use and create spectral irradiance data to account for the fact that the solar spectrum is not the same across the globe and changes over the course of a day. The model should also be able to produce a temperature profile within the PV module in order to visualise how the PCM can be used as a heat sink to keep the temperature of the solar cell within the module as low as possible during high irradiance hours.

1.4. Structure of this thesis

The thesis is structured to explain why there is a need for a thermal model of a PV + PCM system, how this model works and to reflect on its effectivity. Chapter 2 will provide the required background to understand the workings of the model. Chapter 3 focusses on how the model is built up, and how it operates. In chapter 4 the model is validated against measured values and in chapter 5 these validations are discussed. Finally chapter 6 explains where the model can be applied, and where it can be improved upon.

2

Theory and background

In order to create a thermal model of a PV module, it helps to understand how and why a PV module heats up in the first place. This chapter strives to answer those questions and give the background needed to understand how model presented in this thesis operates.

2.1. Electrical energy from the sun

A *solar* panel, as the name would suggest, is used to convert energy coming from the *sun* into electrical energy. This section will give a quick introduction on how light from the sun ends up at the earth's surface and how it is converted into electrical energy.

2.1.1. The solar spectrum

The sun emits an enormous amount of energy, even though it's 148 million kilometres away, the earth receives more than 170 PW ($1.7 \cdot 10^{17}$ W) of solar energy [13]. This energy comes to earth in the form of electromagnetic radiation, also called photons. These photons are sent out at different wavelengths, from ultraviolet to visible light to infra-red. At different wavelengths, different amounts of photons are emitted. This distribution of photons has a characteristic shape and referred to as *the solar spectrum*. In figure 2.1 the solar spectrum is shown as it reaches the earth's atmosphere and how it is transformed as has travelled through the atmosphere to reach ground level.

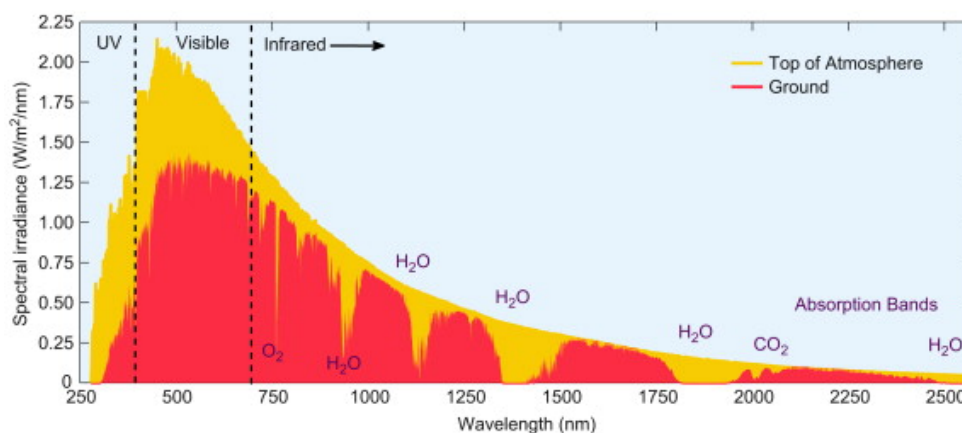


Figure 2.1: The solar spectrum, both at the top of the atmosphere and at ground level [14].

2.1.2. Reflection, absorption and transmission of light

After light from the sun penetrates the atmosphere it reaches, for instance, a PV module. At the glass surface of the PV module three things happen: a part of the light is reflected off the glass, another part gets absorbed by the glass and the rest is transmitted through the glass. This process of reflecting, absorbing and transmitting happens at every layer of the PV module (schematically shown in figure 2.2).

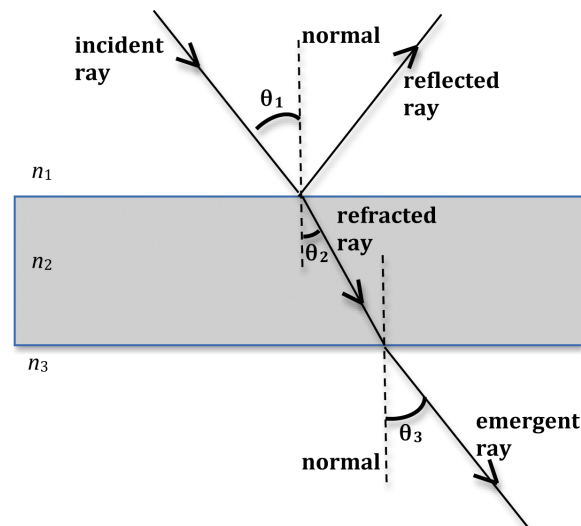


Figure 2.2: Schematic representation of the transmission, reflection and refraction of light as it traverses several media [15]. In the case of a PV module, n_1 could be air, n_2 glass and n_3 the solar cell material or its encapsulant.

The amount of light that is absorbed by a material depends on two factors, the absorption spectrum and the absorption coefficient. The absorption spectrum shows what wavelengths of light will be passed through the material and which will be absorbed. The absorption coefficient how far light of a specific wavelength can penetrate the material.

2.1.3. From absorbed light to electrical energy

When a photon finally reaches the silicon inside the solar cell, it still needs to be converted into electrical energy, also known as electrons. To understand this conversion, some knowledge of how electrons behave in solid materials is required. Within a material, electrons circle their atoms at very specific energy levels. Each atom can hold a certain number of electrons in a stable way. Imagine an empty bucket, the bucket represents the atoms of a material. Water is now added to the bucket, drop by drop, each drop representing an electron. If the bucket is now filled to its fullest point we have a stable material, all atoms having their stable amount of electrons. This fully filled bucket is called the valence band. If a new droplet of water is now introduced, the bucket will flow over. Depending on the type of material something different will happen to this droplet.

In a conductor (metals), this droplet can freely move over the surface of the water. In other words an 'extra' electron in a metal can move freely at an energy level above the valence band, it is now in the conduction band (figure 2.3A). In an insulator, on the other hand, the droplet has nowhere to go since the first energy level above the valence band is very high (figure 2.3B). Because of this high energy barrier, electrons are not able to travel through an insulator. Apart from conductors and insulators there are also semiconductors (like the silicon inside a PV cell). In a semiconductor the conduction band is not directly above the valence band as in a conductor, yet also not as high as in an insulator (see figure 2.3C).

This means that trying to run a current (electrons) through a semiconductor will not be very useful, since the electrons need to cross a high energy barrier in order to travel through the material. There is

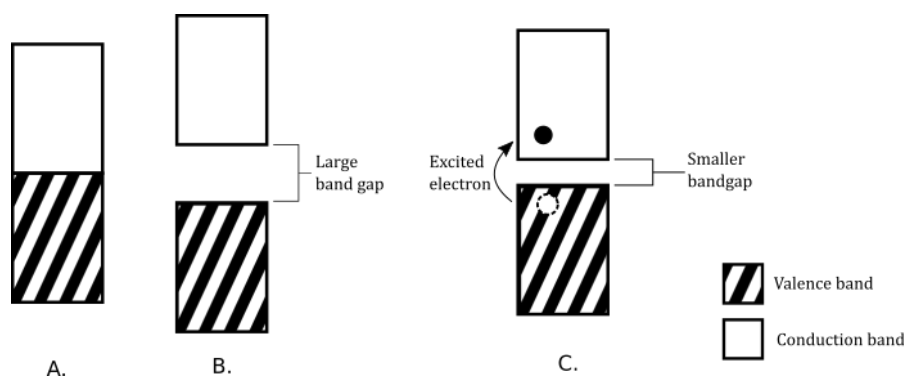


Figure 2.3: Schematic representation of the band gap in a: A. Conductor, B. Insulator and C. Semiconductor. For the semiconductor it is shown how when an electron is excited to the conduction band, a "hole" stays behind in the valence band (adapted from [16]).

another possibility, however. If an electron from the valence band is excited, with a photon for instance, it can move into the conduction band (leaving a vacancy in the valence band, a so called 'hole'). Once it is in the conduction band it can move around freely in the material until it falls back into the valence band. If these electrons and holes are separated and removed from the semiconductor, the electron can be run through an electric circuit, creating electrical current. In this way an incoming photon is converted to electrical current.

2.2. Heat generation in a solar cell

2.2.1. From absorbed light to heat

In a solar cell not all electrons that get excited to the conduction band are able to leave the semiconductor, most of them quickly recombine with a hole left behind. Recombination can be seen as the opposite of exciting an electron into the conduction band, so instead of electro-magnetic radiation 'creating' an electron, an electron 'creates' electro-magnetic radiation (heat or light). In a solar cell recombination generates heat, but in an LED recombination is used to create light.

Not all photons that reach a solar cell have the exact energy required to excite an electron out of the valence band, some will have more and some less energy. If the photon does not have enough energy, it will still be absorbed by the solar cell, but as *thermal* energy. If the photon has too much energy the electron will "overshoot", high up into the conduction band. An energy with that much energy is not stable within the material and quickly "cools down" to a lower energy level, releasing thermal energy in the process (this is called thermalisation). A typical c-Si solar cell has an efficiency of around 15-18% [17], which means that 82-85% of incoming energy is converted into thermal energy.

2.2.2. Effect of temperature on cell efficiency

The performance of a solar cell is often deduced from its IV-curve. Such a curve shows the amount of current that can be extracted from an illuminated solar cell for all voltages between zero and the open-circuit voltage (V_{oc}). The open-circuit voltage is the maximum amount of voltage available from a solar cell, this happens when there is no current (in other words: an open circuit). The current is at its maximum when there is no voltage over the cell, this is called the short-circuit current, I_{sc} .

A solar cell's performance is dependant on it's temperature. To be more specific: increasing the cell temperature slightly increases the short-circuit current of the solar cell, while greatly reducing the open-circuit voltage (see figure 2.4). So if the temperature of a solar cell is high, its efficiency is reduced and less efficient energy conversion leads to more of the incoming light being converted into heat, not electrical energy. This, combined with the fact that high temperatures and temperature fluctuations

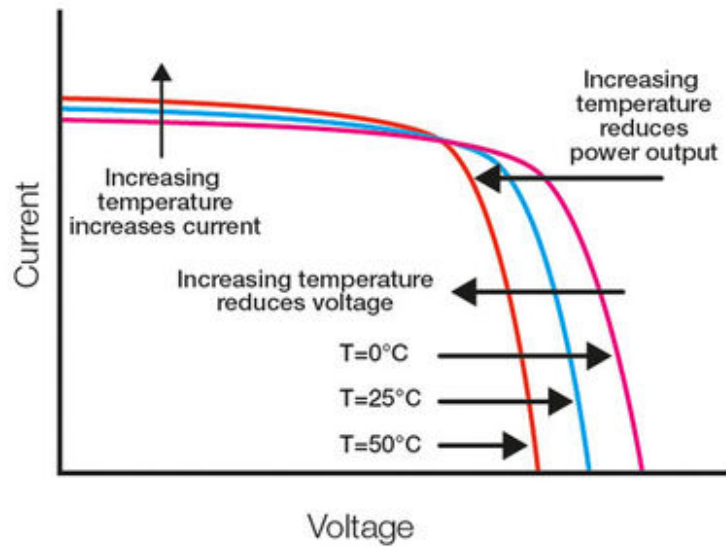


Figure 2.4: The effect of temperature on the IV curve of a solar cell [18].

cause irreversible damage to a solar cell, means that cooling of a solar cell is key.

2.3. Heat transfer and cooling methods

To understand how the heat generated within a solar module moves throughout the module, we turn to heat transfer theory. Basically, *"Whenever there exists a temperature difference in a medium or between media, heat transfer must occur"* [19]. There are three different types of heat transfer: conduction, convection and radiation. Conduction is the transfer of heat through a solid or a stationary fluid. Convection takes place when there is heat transfer between a surface and a moving fluid (or gas). Radiation is the transfer of heat that takes place because all objects emit energy through electromagnetic radiation. This section quickly runs through these three heat transfer mechanisms and with that knowledge some currently researched cooling methods are examined.

2.3.1. Conduction

If there is a temperature difference within one (solid) material, conduction takes place. The amount of heat transferred (one dimensionally) in this way can be calculated as follows:

$$q_x = -kA \frac{dT}{dx} \quad (2.1)$$

Where q_x (W) is the heat rate in the x direction, k (W/mK) is the thermal conductivity of the material, A the area perpendicular to the heat flow and $\frac{dT}{dx}$ is the temperature gradient. This rate equation is also known as Fourier's law.

2.3.2. Convection

Convection takes place at the surface of an object, where it comes into contact with moving gasses or liquids. Within the context of this thesis convection refers to the the heat transfer between the system and the air around it. The rate of this transfer is determined in the following way:

$$q_x = hA(T_{surface} - T_{air}) \quad (2.2)$$

Where h (W/m²K) is the *convection heat transfer coefficient*, A the area of the surface, $T_{surface}$ the temperature of the surface and T_{air} the temperature of the air surrounding the module. The coefficient h depends on many factors, including but not limited to object geometry, wind speed, wind direction, air viscosity and surface roughness. It comes as no surprise that many simplifications are available (which, in turn, also range in complexity) [20]. For this thesis the h value for the front of the PV module is

$$h = 2.8 + 3 \cdot w \quad (2.3)$$

which is a simple convection heat transfer coefficient model originally calculated for solar collectors by Watmuff et al. [21], where w is the measured wind speed in m/s.

2.3.3. Radiation

Lastly, heat can be transferred through the emission of energy from an object's surface. Any surface emits energy due to the thermal motion of particles within the material. Opposed to conduction and convection, no medium is required for radiative heat transfer. The heat transfer rate due to radiation is calculated as such:

$$q_x = \epsilon\sigma A(T_{surface}^4 - T_{surroundings}^4) \quad (2.4)$$

Where ϵ is the emissivity of the material, which has a value between 0 and 1. σ is the Stefan-Boltzmann constant ($5.67 \cdot 10^{-8}$ W/m²K⁴).

2.3.4. Cooling methods

Both sections 1.2 and 2.2.2 have described high temperatures within a PV module as problematic. Research has come up with ample ideas of cooling down PV modules[22]. These ideas can be sorted into two fields: active cooling and passive cooling. Active cooling requires energy to be put into the system to be able to cool the PV module. Examples of active cooling are: water cooling, active heat pipes or forced airflow cooling. A passive system requires no external energy, examples are: passive heat sinks, radiative cooling, spectral filters or the use of phase change materials. Below a few examples and their effectiveness are highlighted, but note that there are many innovative ways of thermal management of PV modules being researched at the moment.

Passive Heat sinks A popular method for passively cooling PV modules, is the use of passive heat sinks, mostly in the form of metal fins. These fins increase the surface area at the back of the PV module, so more convective cooling can take place. The performance of these fins has shown to be very dependant on how much air can flow passed the fins [23].

Water cooling A PV module can be cooled by pumping water through pipes at the back of the module. Yet, another method using water that has been proven to be very effective in reducing the module temperature is spraying the the module with water (with temperature reductions up to 26°C[23]).

Radiative cooling The previously mentioned cooling methods all rely on conduction and convection as its heat transfer mechanisms, what kind of cooling can be achieved by the means of radiative heat transfer? By increasing the emissivity of the surface of the module, radiative heat transfer is increased. The benefits gained by this have been rather disappointing [22].

Selective reflection Another way of increasing the amount of heat radiated by a PV module, is to increase the reflection of wavelengths that will not be used to produce electrical energy (in other words, the use of optic filters). There are two main forms of optic filters used for PV applications: infra-red (IR) filters (that reflect IR radiation, not transmit it) and multi-functional filters. IR filters have shown cooling capacity of up to 6°C in a hot climate [24]. Multi-functional (colour) filters, which try to reduce thermalisation losses (losses that occur from electrons 'overshooting' the band gap, see section 2.2.1) have been shown to reduce module temperatures up to 12°C. However, since these filters partly reflect visible light (hence the colour) less photons reach the solar cell, resulting in substantial reductions on the energy yield [25].

2.4. Phase Change Materials as cooling method

As mentioned before, one innovative way to passively cool a PV module, that has become a popular topic in recent years [26], is the use of Phase Change Materials (PCMs). Every material can change phase, yet a material is deemed a PCM when it can absorb or release enough energy to be useful. During phase transition the temperature of a material remains (somewhat) constant, the energy required to change phase is called latent heat. The counterpart of latent heat is sensible heat which is the amount of energy required to bring a material up to a specific temperature. In figure 2.5 the relation between sensible and latent heat is schematically shown. Because phase change takes a lot of energy, a PCM can be an interesting alternative to a passive heat sink (which only heats up by means of sensible heat). PV-PCM systems have shown great potential thus far, with temperature reductions up to 10°C [27] and efficiency improvements up to 7.8% [28]. These improvements are quite high compared to other passive cooling methods [22]. The optic filters discussed in section 2.3.4, for example, reach comparable numbers of temperature reduction, but pay with a reduction in energy yield. Since the PCM is installed at the back surface of the PV cell, there is no decrease in energy yield.

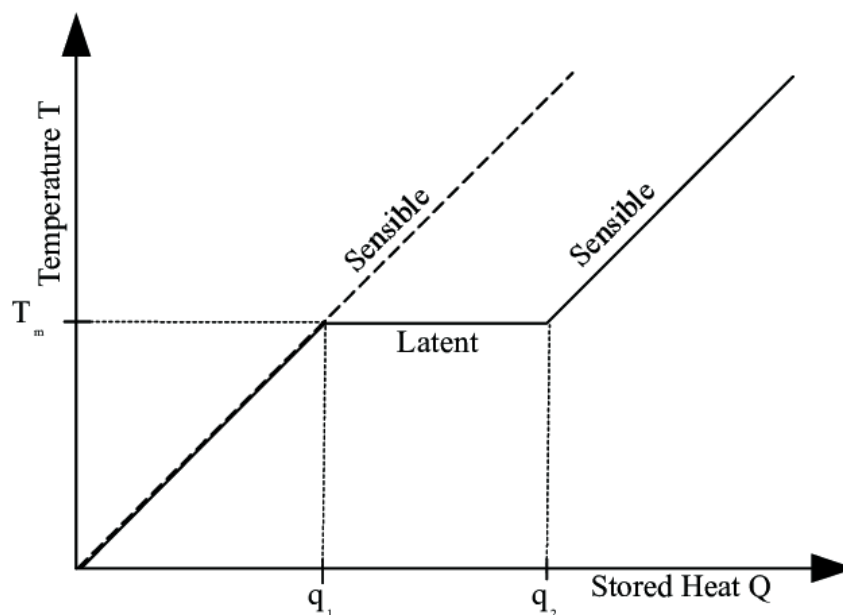


Figure 2.5: Using the latent heat of a PCM, more energy can be stored. In other words, more heat from the solar cell can be absorbed, compared to using a material that does not change phase (indicated by the dotted line) [29].

To incorporate phase change in the heat transfer equations mentioned in section 2.3 , one can look at the total enthalpy of a PCM. This enthalpy can be described as

$$H = h + L \cdot f_l \quad (2.5)$$

Where h is the enthalpy to bring the material up to the desired temperature (the sensible heat) and $L \cdot f_l$ is the energy required for phase change (the latent heat). L is the latent heat of fusion (J/kg) and f_l is the local liquid fraction, which is 1 when fully liquid and 0 when fully solid. The sensible enthalpy is defined as

$$h = \int_{T_m}^T c_p dT \quad (2.6)$$

where c_p (J/KgK) is the specific heat capacity. When the sensible enthalpy is differentiated in time it gives

$$\frac{\delta h}{\delta t} = c_p \cdot \frac{\delta T}{\delta t} \quad (2.7)$$

A change in internal energy ΔQ (J) in a slice of a material can be calculated as follows.

$$\Delta Q = A \cdot \rho \cdot c_p \cdot dx \cdot \Delta T \quad (2.8)$$

with ρ (kg/m³) the density of the material, c_p (Jkg⁻¹K⁻¹) the specific heat capacity and ΔT (K) the change in temperature.

combining this with equation 2.1 gives the heat equation in one dimension.

$$\frac{\delta T}{\delta t} = \frac{k}{\rho \cdot c_p} \frac{\delta^2 T}{\delta x^2} \quad (2.9)$$

When equation 2.7 is substituted into equation 2.9, the following equation is obtained:

$$\frac{\delta H}{\delta t} = \frac{k}{\rho} \frac{\delta^2 T}{\delta x^2} \quad (2.10)$$

substituting equation 2.5 into 2.10 gives

$$\frac{\delta h}{\delta t} = \frac{k}{\rho} \frac{\delta^2 T}{\delta x^2} - L \frac{\delta f_l}{\delta t} \quad (2.11)$$

substituting 2.7 into equation 2.11 now gives the heat equation that incorporates the PCM that will be used to model PCM temperatures in this thesis (equation 2.12).

$$\frac{\delta T}{\delta t} = \frac{k}{\rho c_p} \frac{\delta^2 T}{\delta x^2} - \frac{L}{c_p} \frac{\delta f_l}{\delta t} \quad (2.12)$$

3

A one-dimensional spectrally resolved thermal model

To be able to study the potential of PCMs as passive temperature management for PV modules, this thesis will present a one-dimensional, spectrally resolved transient thermal model. The model is one-dimensional in order to reduce computation times and complexity. The use of a one-dimensional model is justified since heat transfer in a PV module mainly happens in one direction, from the front to the back surface. Spectrally resolved means that the model uses spectral input data in its calculations of module temperatures. Finally, the model is transient (as opposed to steady-state), in order to better understand the heating and cooling processes inside a PV module.

3.1. Nodal Network and variable mesh algorithm

A transient model calls for a discretisation in both time and space. The system will be discretised in space by dividing a one-dimensional representation of the PV module into control volumes. At the centre of each control volume is a node, each node represents the temperature (and any other physical parameter) of the control volume. Together these nodes create a nodal network. Since the system (PV + PCM) consists out of layers with a large variance of thickness (microns to centimetres), the network should be able to have variable distances between nodes. This thesis introduces an algorithm of creating this nodal network, or "mesh". The input for this "mesh maker", is the thickness of each layer and the amount of nodes the user wants in each layer. When the amount of nodes in a layer is known, looking at figure 3.1, we can define the thickness of the last layer as follows:

$$d_N = (n_N - \frac{1}{2}) \cdot \Delta x_N \quad (3.1)$$

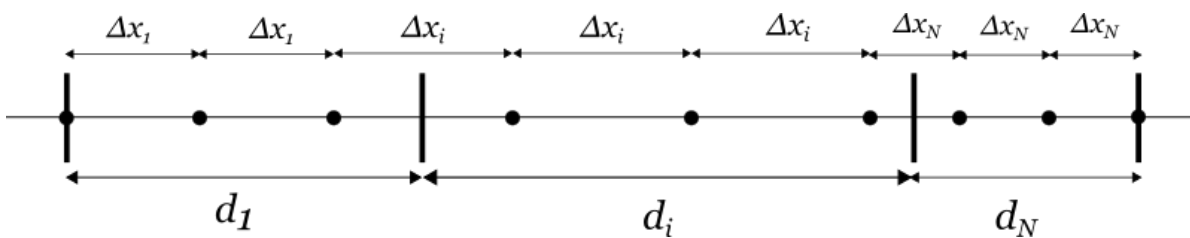


Figure 3.1: Schematic example of the relation between the layer thickness d , the spacial increments, Δx , and the amount of nodes in each layer. In this example there are three nodes in each layer, $i = 2$ and $N = 3$.

where d_N is the layer thickness, n_N the number of nodes assigned to the layer and Δx_N the associated space increment. Going from right to left, the thickness of the following layers can be defined as

$$d_i = (n_i - \frac{1}{2}) \cdot \Delta x_i + \frac{1}{2} \Delta x_{i+1} \quad (3.2)$$

and finally the first layer thickness as

$$d_1 = (n_1 - 1) \cdot \Delta x_1 + \frac{1}{2} \Delta x_2 \quad (3.3)$$

These equations can be arranged as a matrix equation that is shaped thusly,

$$\begin{bmatrix} n_1 - 1 & \frac{1}{2} & 0 & 0 & 0 \\ 0 & \ddots & \ddots & 0 & 0 \\ 0 & 0 & n_i - \frac{1}{2} & \frac{1}{2} & 0 \\ 0 & 0 & 0 & \ddots & \ddots \\ 0 & 0 & 0 & 0 & n_N - \frac{1}{2} \end{bmatrix} \cdot \begin{bmatrix} \Delta x_1 \\ \vdots \\ \Delta x_i \\ \vdots \\ \Delta x_N \end{bmatrix} = \begin{bmatrix} d_1 \\ \vdots \\ d_i \\ \vdots \\ d_N \end{bmatrix} \quad (3.4)$$

This matrix equation can be solved with an algorithm like the Gauss-Siedel method, giving the Δx values for every layer. The Δx values are the distances between nodes for a specific layer, as can be seen in figure 3.1. In other words, the user provides the thickness of each layer and the number of nodes they want in each layer, the algorithm then provides the distances between all the nodes in order to fit into their layers. A problem can arise at the first or at a middle layer, since

$$\Delta x_i = \frac{d_i - \frac{1}{2} \Delta x_{i+1}}{n_i - \frac{1}{2}} \quad (3.5)$$

Where

$$d_i - \frac{1}{2} \Delta x_{i+1} > 0, \text{ so} \quad (3.6)$$

$$\Delta x_{i+1} < 2d_i \quad (3.7)$$

Since Δx_i would become negative otherwise. When this is the case, there are two courses of action. One is to change the amount of nodes required for each layer in such a way that Δx_{i+1} becomes smaller (the more nodes the user requires in a layer, the smaller the distance between them has to be). The other is to merge two layers together. If a merge is needed, the physical parameters of the merged node will be calculated according to the weight that each of the merged materials have inside the node.

The thickness of a control volume i generally is Δx_i except at the edges of the module where it is $\frac{1}{2} \Delta x_i$ or between two different Δx where the thickness is (see figure 3.2 also).

$$d_{cv} = \frac{\Delta x_1}{2} + \frac{\Delta x_2}{2} \quad (3.8)$$

note that d_{cv} is different to the d_i seen before. The control volume thickness, d_{cv} , is the space around a node, while layer thickness, d_i , is the thickness of a complete layer consisting out of one material.

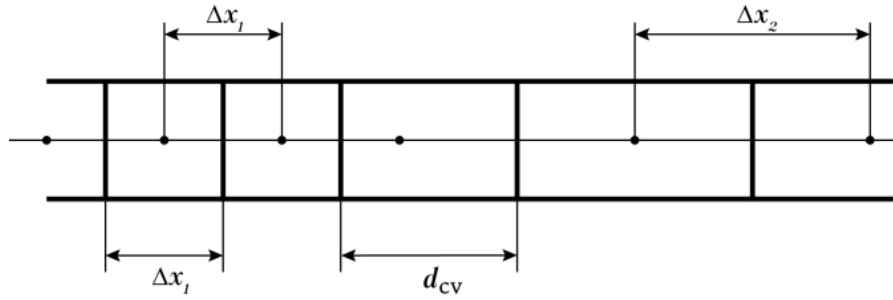


Figure 3.2: Between to differently sized space increments Δx , the control volume has a different thickness than the usual $d_{cv} = \Delta x$

3.2. Energy Balance Method

Due to the conservation of energy the sum of all the heat that enters, leaves or is generated within one control volume should be equal to the difference in energy within one time step.

For a one dimensional model this means the following

$$(q_{left} + q_{right} + q_{gen}) \cdot \Delta t = \Delta Q \quad (3.9)$$

$$q_{left} + q_{right} + q_{gen} = \rho \cdot V_{cv} \cdot c_p \cdot \frac{\Delta T}{\Delta t} \quad (3.10)$$

Where q_{left} and q_{right} (W) are the heat rates of energy entering or leaving the control volume, q_{gen} (W) is the heat being produced within the control volume and ΔQ (J) is the difference in energy within one time step, Δt (s). ρ (kg/m³) is the density of the material within the control volume, V_{cv} (m³) is the volume of the control volume and c_p (J/kgK) is the specific heat capacity at constant pressure.

For a node at the i^{th} position that does not belong to a surface, q_{left} and q_{right} can be substituted by eq. 2.1, when $\frac{dT}{dx}$ is replaced by $\frac{\Delta T}{\Delta x}$ this results in

$$\rho \cdot V_{cv} \cdot c_p \cdot \frac{\Delta T}{\Delta t} = kA \cdot \frac{T_{i-1} - T_i}{\Delta x_{i-1}} + kA \cdot \frac{T_{i+1} - T_i}{\Delta x_i} + q_{gen} \quad (3.11)$$

Where k (W/mK) is the thermal conductivity, T_i (K) is the temperature of the node and T_{i-1} and T_{i+1} are the temperatures of the node to the left and right respectively. There is one caveat to this equation, when node $i - 1$ is made out of a dissimilar material compared to node i (or i compared to $i + 1$) one cannot use the same value for k .

To take this difference in k -values into account it helps to think in terms of *thermal resistance*. Let's rewrite the heat rate equation of conductive heat transfer with the node to the right

$$q_{right} = kA \frac{T_{i+1} - T_i}{\Delta x_i} = \frac{T_{i+1} - T_i}{\Delta x_i / kA} = \frac{T_{i+1} - T_i}{R_t} \quad (3.12)$$

Where R_t is the thermal resistance. Now when the k -value of node i (let's call it k_A) is different than that of node $i + 1$ (k_B), the thermal resistance can be rewritten as

$$R_t = \frac{\Delta x_i}{k_A A} + \frac{\Delta x_i}{k_B A} \quad (3.13)$$

The volume of a control volume, V_{cv} , can be written as $A \cdot d_{cv}$, where d_{cv} is the thickness of the control volume (see eq. 3.8). Now equation 3.11 can be rewritten as

$$\frac{\Delta T}{\Delta t} = \frac{k}{\rho C_p d_{cv}} \frac{T_{i-1} - T_i}{\Delta x_{i-1}} + \frac{k}{\rho C_p d_{cv}} \frac{T_{i+1} - T_i}{\Delta x_i} + \frac{q_{gen}}{\rho C_p V_{cv}} \quad (3.14)$$

In this equation $\frac{k}{\rho C_p}$ is known as the thermal diffusivity α (m^2/s). Substituting this and rearranging results in the following.

$$\Delta T = \frac{\alpha \Delta t}{\Delta x_{i-1} \cdot d_{cv}} \cdot (T_{i-1} - T_i) + \frac{\alpha \Delta t}{\Delta x_i \cdot d_{cv}} \cdot (T_{i+1} - T_i) + \frac{\alpha \Delta t}{k \cdot V_{cv}} \cdot q_{gen} \quad (3.15)$$

Since $\Delta T = T_i - T_i^{old}$, with T_i^{old} the temperature of node i from the last time step, this can be written in a more generalised form:

$$a_{i-1}T_{i-1} + a_iT_i + a_{i+1}T_{i+1} = b_i \quad (3.16)$$

$$\text{with } a_{i-1} = \frac{-\alpha \Delta t}{d_{cv} \cdot \Delta x_{i-1}}, a_{i+1} = \frac{-\alpha \Delta t}{d_{cv} \cdot \Delta x_i}, a_i = 1 + \left(\frac{1}{\Delta x_{i-1}} + \frac{1}{\Delta x_i} \right) \frac{\alpha \Delta t}{d_{cv}} \text{ and } b_i = T_i^{old} + \frac{\alpha \Delta t}{k V_{cv}} \cdot q_{gen}.$$

Boundary equations At the surfaces, convection and radiation need to be taken into account. The equation at the first node ($i = 1$) is denoted as follows

$$\rho \cdot V_{cv} \cdot c_p \cdot \frac{\Delta T}{\Delta t} = h(t)A(T_a - T_1) + \epsilon \sigma (T_{surroundings}^4 - T_1^4) + kA \cdot \frac{T_2 - T_1}{\Delta x_1} \quad (3.17)$$

Where $h(t)$ is the convection heat transfer coefficient (W/m^2K) for every time step, T_a the ambient temperature outside the module this can be the same as $T_{surroundings}$, but is not necessarily the case. Note that the last term in equation 3.17 is the conduction with the next node, similar to equation 3.11, yet now with $i = 1$ and $i + 1 = 2$. This equation will also be formalised, similar to eq. 3.16. Starting with dividing by V_{cv} , ρ and c_p , and substituting V_{cv} with $A \cdot \frac{1}{2} dx_1$. From here on out $T_{surroundings}$ is also abbreviated as T_{sur}

$$\frac{\Delta T}{\Delta t} = \frac{2h(t)}{\rho C_p dx_1} (T_a - T_1) + \frac{2\epsilon \sigma}{\rho C_p dx_1} (T_{sur}^4 - T_1^4) + \frac{k}{\rho C_p dx_1^2} (T_2 - T_1) + \frac{q_{gen}}{\rho C_p V_{cv}} \quad (3.18)$$

When this is divided by Δt , the Fourier number ($Fo = \frac{\alpha \Delta t}{dx_1^2}$, with $\alpha = \frac{k}{\rho C_p}$) and the Biot number ($Bi(t) = \frac{h(t)}{k} dx_1$) can be substituted into the equation, producing

$$\Delta T = 2FoBi(t)(T_a - T_1) + \frac{2\epsilon \sigma \alpha \Delta t}{k dx_1} (T_{sur}^2 - T_1^2) + 2Fo(T_2 - T_1) + \frac{2\alpha q_{gen} \Delta t}{k V_{cv}} \quad (3.19)$$

To formalise this further into the shape of eq. 3.16, the radiation term needs to be modified to a linear expression. This can be achieved by rewriting $T_{sur}^4 - T_1^4$ as $(T_{sur}^2 - T_1^2)(T_{sur} + T_1)(T_{sur} - T_1)$. $(T_{sur}^2 - T_1^2)(T_{sur} + T_1)$ changes less than 5% when T_1 changes 10 °C, so if T_1^{old} (temperature of T_1 in the last time step) is used, the factor can be made into a constant:

$$C_{rad} = \frac{2\epsilon \sigma \alpha \Delta t}{k dx_1} (T_{sur}^2 + (T_1^{old})^2)(T_{sur} + T_1^{old}) \quad (3.20)$$

Now the heat equation at the surface can be rewritten to

$$a_1 T_1 + a_2 T_2 = b_1 \quad (3.21)$$

With $a_1 = 1 + 2Fo + 2FoBi(t) + C_{rad}$, $a_2 = -2Fo$ and $b_1 = T_1^{old} + 2FoBi(t)T_a + C_{rad}T_a + \frac{2\alpha q_{gen}\Delta t}{kV_{cv}}$.
For the surface on the other side of the module, the formalised equation becomes

$$a_{N-1} T_{N-1} + a_N T_N = b_N \quad (3.22)$$

with a_{N-1} similar to a_2 , a_N similar to a_i and b_N similar to b_i , only the physical parameters need to be adjusted.

3.3. Internal heating using SMARTS and GenPro4

In the previous section one value remains to be filled in, q_{gen}/V_{cv} , which is the volumetric internal heat rate (W/m^3). This section aims to explain how the amount of heat generated in each node is calculated in a spectrally resolved way using several software packages. The calculation can be divided into four parts: calculating the solar position, calculating the solar spectrum, calculating the amount of absorption in each layer and finally determining the electrical efficiency within the silicon layer.

The position of the sun is calculated using the Solar Position Algorithm (SPA) (made by NREL[30]), this algorithm very accurately calculates the position of the sun based on geographical location and set-up characteristics. The azimuth and zenith of the sun for each time step (obtained by SPA) are used as the input for the Simple Model of the Atmospheric Radiative Transfer of Sunshine (SMARTS, version 2.9.5 [31]). This model calculates the spectrum of the sun based on a vast array of inputs (such as atmosphere, albedo and pollution data). The Normalised Global Tilted spectrum from SMARTS can now be multiplied with a measured value of irradiance in order to create spectral irradiance data. To calculate the amount of light that is absorbed within each layer for every wavelength GenPro4[32] is used. With the spectral irradiance for each time step from SMARTS and the absorption per layer per wavelength from GenPro, the amount of energy absorbed within each layer can be calculated. Lastly using the temperature coefficient of the cell combined with the temperature of the last time step, the efficiency of the cell is calculated, and therefore the amount of energy that is turned into heat within the cell, giving q_{gen} for every time step.

3.4. Input overview

The previous sections have explained all the data and calculations required before the model starts solving. An overview is shown in figure 3.3. In this flowchart 'location data' refers to the geographical coordinates of the module, its elevation, rotation and tilt.

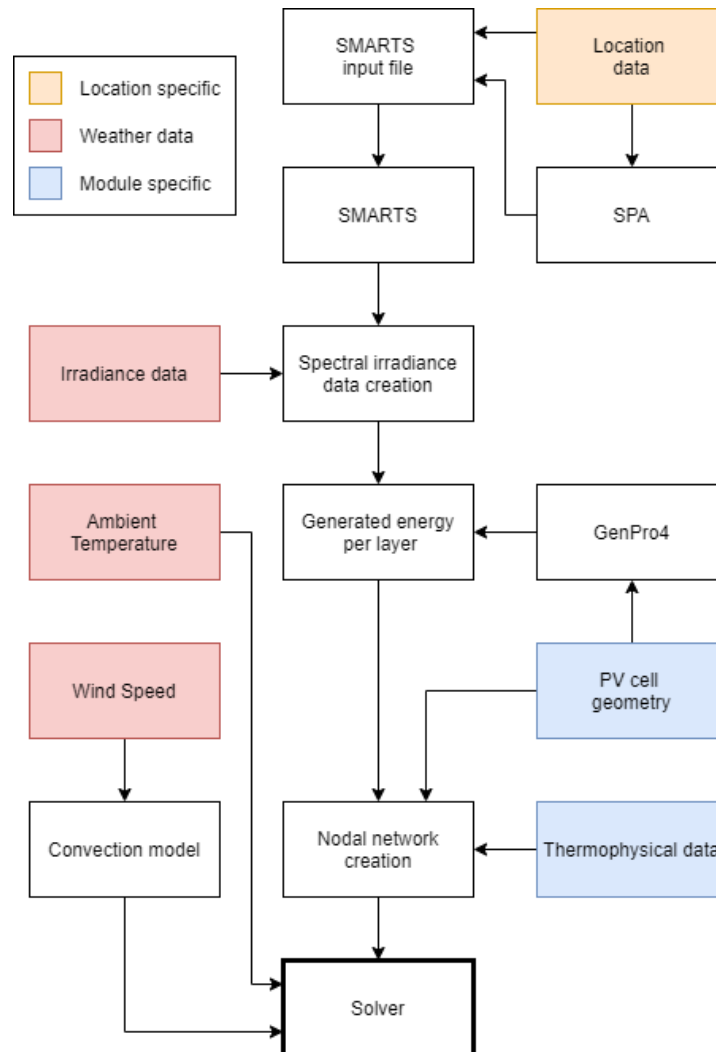


Figure 3.3: A flowchart depicting all the calculations and data required for the main solver of the model.

3.5. PCM model

The PCM model used in this thesis is based on the work of Zivkovic et al.[33]. This model is based upon a number of assumptions

1. The effects of convection while melting will be ignored, since they are negligible
2. The PCM will change phase isothermally
3. The physical properties of the PCM can differ between liquid and solid phase, but are independent of temperature
4. The PCM is homogeneous and isotropic

Within the PCM the heat equation is a discretisation of eq. 2.12 in a similar way as eq. 3.14.

$$\frac{\Delta T}{\Delta t} = \frac{k}{\rho c_p d_{cv}} \cdot \frac{T_{i-1} - T_i}{\Delta x_{i-1}} + \frac{k}{\rho c_p d_{cv}} \cdot \frac{T_{i-1} - T_i}{\Delta x_i} - \frac{L_H}{c_p} \cdot \frac{\Delta f}{\Delta t} \quad (3.23)$$

Where L_H (J/kg) is the latent heat of fusion and Δf is the change in the liquid fraction. The liquid fraction, f , is a value between 0 (fully solid) and 1 (fully liquid) and is given by

$$f = \begin{cases} 1 & \text{if } T_i > T_m \\ f & \text{if } T_i = T_m \\ 0 & \text{if } T_i < T_m \end{cases} \quad (3.24)$$

Where T_m is the melting temperature of the PCM. There can be two cases when solving equation 3.23, The PCM is either changing phase or it is not. If it is not changing phase, there is no change in liquid fraction, hence $\Delta f = 0$. Without a change in liquid fraction the heat equation is simplified in the same way as equation 3.16. If the material is changing phase, however, $T = T_m$ so $\Delta T = 0$ and equation 3.23 can be solved for f (see equation 3.25). The coefficients seen in eq. 3.16 then become $a_{i-1} = a_{i+1} = 0$, $a_i = 1$ and $b_i = T_m$. Resulting in $T_i = T_m$, for a control volume that is in the process of melting. The next section will explain how the model comes to a solution step by step.

$$f_i = f_i^{old} + \frac{k\Delta t}{\rho L_H d_{cv}} \left(\frac{T_{i-1}}{\Delta x_{i-1}} - \left(\frac{1}{\Delta x_{i-1}} + \frac{1}{\Delta x_i} \right) T_m + \frac{T_{i+1}}{\Delta x_i} \right) \quad (3.25)$$

3.6. Solving methodology

The previous sections have shown that the heat equation at any node can be rearranged into the following form.

$$a_{i-1}T_{i-1} + a_iT_i + a_{i+1}T_{i+1} = b_i \quad (3.26)$$

This creates a system of equations and can be translated into a matrix operation of the form

$$\begin{bmatrix} a_{1,1} & a_{1,2} & 0 & 0 & 0 \\ a_{2,1} & a_{2,2} & a_{2,3} & 0 & 0 \\ 0 & \ddots & \ddots & \ddots & 0 \\ 0 & 0 & 0 & a_{N,N-1} & a_{N,N} \end{bmatrix} \begin{bmatrix} T_1 \\ T_2 \\ \vdots \\ T_N \end{bmatrix} = \begin{bmatrix} b_1 \\ b_2 \\ \vdots \\ b_N \end{bmatrix} \quad (3.27)$$

this system can be solved for the T vector, which will give the temperature profile inside the PV module for one time step. However, some of the nodes in this system represent a PCM that can melt or solidify. An algorithm is created to ensure this happens correctly and will be explained in detail below.

1. for all non-PCM nodes the a coefficients are defined. For the PCM nodes, if the liquid fraction of a PCM node is in the interval $0 < f_i < 1$, $a_{i-1} = a_{i+1} = 0$, $a_i = 1$ and $b_i = T_m$. For the surface nodes b_i is calculated from the measured wind speed and ambient temperature.
2. The matrix equation 3.27 is solved.
3. Liquid fractions are updated using equation 3.25.
4. A check is performed to see if melting or solidifying has started or ended in a node. If this is the case, the a and b values need to be updated and step 1 to 3 will be run through again.

when in step 4 the beginning or ending of melting or solidifying is detected, some values need to be updated. Every case will be discussed now.

Beginning of melting or solidifying When $T_i \geq T_m$ while $T_i^{old} < T_m$ (start of melting), OR $T_i \leq T_m$ while $T_i^{old} > T_m$ (start of solidifying), control volume i has started changing phase in this time step. The coefficients a_{i-1} , a_i , a_{i+1} and b_i will be changed. However, the liquid phase calculation according to eq. 3.25, is modified to

$$f_i = f_i^{old} + \frac{k\Delta t}{\rho L_H d_{cv}} \left(\frac{T_{i-1}}{\Delta x_{i-1}} - \left(\frac{1}{\Delta x_{i-1}} + \frac{1}{\Delta x_i} \right) T_m + \frac{T_{i+1}}{\Delta x_i} \right) - \frac{c_p}{L} (T_m - T_i^{old}) \quad (3.28)$$

for the first time step the control volume is changing phase. The last term in eq. 3.28 is the amount of heat needed to get the control volume exactly to the melting temperature.

End of melting When for a control volume it is calculated that $f_i \geq 1$ while $f_i^{old} < 1$, melting has ended. The coefficients a_{i-1} , a_i and a_{i+1} are set to non-phase change values. For the next time step $b_i = T_m \frac{L}{c_p} (1 - f_i^{old})$, to account for the amount of heat needed to get the liquid fraction from f_i^{old} to 1.

End of solidifying When for a control volume it is calculated that $f_i \leq 0$ while $f_i^{old} > 0$, solidifying has ended. Similar to the end of melting the coefficients a_{i-1} , a_i and a_{i+1} are reset, but $b_i = T_m \frac{L}{c_p} (0 - f_i^{old})$.

4

Validation

The following chapter will attempt to validate the one-dimensional thermal model presented in the last chapter. First, the PCM part of the model will be validated on its own with studies from literature. Then the non-PCM part will be used to simulate temperatures of a PV module installed at the TU Delft. With the viability of both the PCM model and the rest of the thermal model studied, they will be combined in order to simulate a PV + PCM system.

4.1. PCM model validation

To get a full picture of the accuracy of the PCM model, it will be tasked with both a melting and solidifying problem. The selected phase change problems have both been used to validate PCM models from other studies [34] [33].

Solidifying

The first validation of the PCM model is done with the use of a one dimensional test problem set out by Voller [35]. The problem is stated as such: "A pure liquid initially at 28°C occupies the semi-infinite space $x \leq 0$. At time $t = 0$ the surface at $x = 0$ is fixed at the temperature of -10°C, which is below the freezing point of the substance $T_m = 0^\circ\text{C}$." Other thermal properties of this liquid are $k = 2$, $\rho c = 2.5 \cdot 10^6$ and $\rho L = 10^8$, these values are the same for both solid and liquid phase. Voller describes that the position of the phase change front should be at $x = 0.8415\text{m}$ after 25 days. The model presented in this thesis calculates the position of the phase change front at 0.8507m, only a 1.1% difference.

Melting

In order to also validate melting of the PCM, the model is validated with a test problem presented by Solomon [36]. Here, a slab of paraffin is subjected to a constant temperature of 95°C at $x = 0$. As can be seen in figure 4.1, the model closely follows the analytical solution to this two-phase problem. The figure also shows that the model produces a very defined phase change front, compared to the more smooth transition shown by the analytical solution. This sharper edge is the result of a_{i-1} and a_{i+1} from equation 3.16 being set to 0 when node i is changing phase, so no conductive heat transfer in or out of the node is calculated at that moment.

By successfully validating the PCM model with both a melting and a solidifying process, it can be assumed that the model will perform correctly in the complete thermal model.

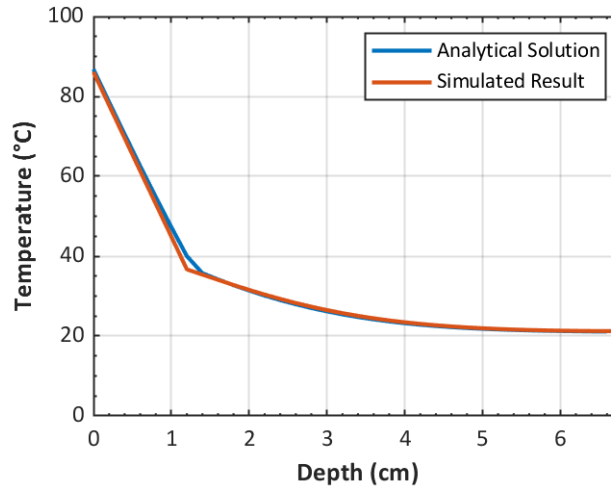


Figure 4.1: Simulation of the melting process of a PCM.

4.2. Note on error calculations

In the following sections the quality of the results from the model will be evaluated with the use of several bias and error calculations. This section will give a quick overview of these calculations and how their results can help to understand the performance of a model.

Mean Absolute Error (MAE) The Mean Absolute Error (MAE) is the *measure of errors between paired observations expressing the same phenomenon*, for this thesis the two observations will be the measured data and the simulated data. The MAE is calculated as

$$\text{MAE} = \frac{\sum_{i=1}^n |P_i - O_i|}{n} \quad (4.1)$$

where P_i are the prediction values and O_i the observations. The MAE gives an impression of the size of the *average* error between the two observations.

Mean Bias Error (MBE) Where the MAE shows the average magnitude of the errors between two observations, the Mean Bias Error (MBE) shows the *direction*. It is calculated as follows:

$$\text{MBE} = \frac{\sum_{i=1}^n (P_i - O_i)}{n} \quad (4.2)$$

The calculation is very similar to that of the MAE, but because of the lack of absolute signs it shows the overall direction (positive or negative) of error between the two observations.

4.3. Validation of the spectral input (SMARTS)

As explained in section 3.3, the model uses SMARTS to obtain spectral data. To confirm that SMARTS is working as intended the results produced by SMARTS are compared to spectral measurements at the PV monitoring station at the TU Delft. For a day with high irradiance (7th of July, 2020) and a day with low irradiance (24th of February, 2020), the SMARTS method is compared to the measured spectrum at three times of the day: near sunrise, when the sun is at its highest point and at sunset. The results

can be seen in figure 4.2. For the most part the SMARTS model follows the measurements, albeit with more discrepancies at sunrise and near sunset. Especially early in the morning on the low irradiance day, SMARTS underestimates the amount of energy in the lower wavelength range, yet overestimates at the higher wavelengths. Note that the model uses the output of SMARTS without taking cloudiness into account.

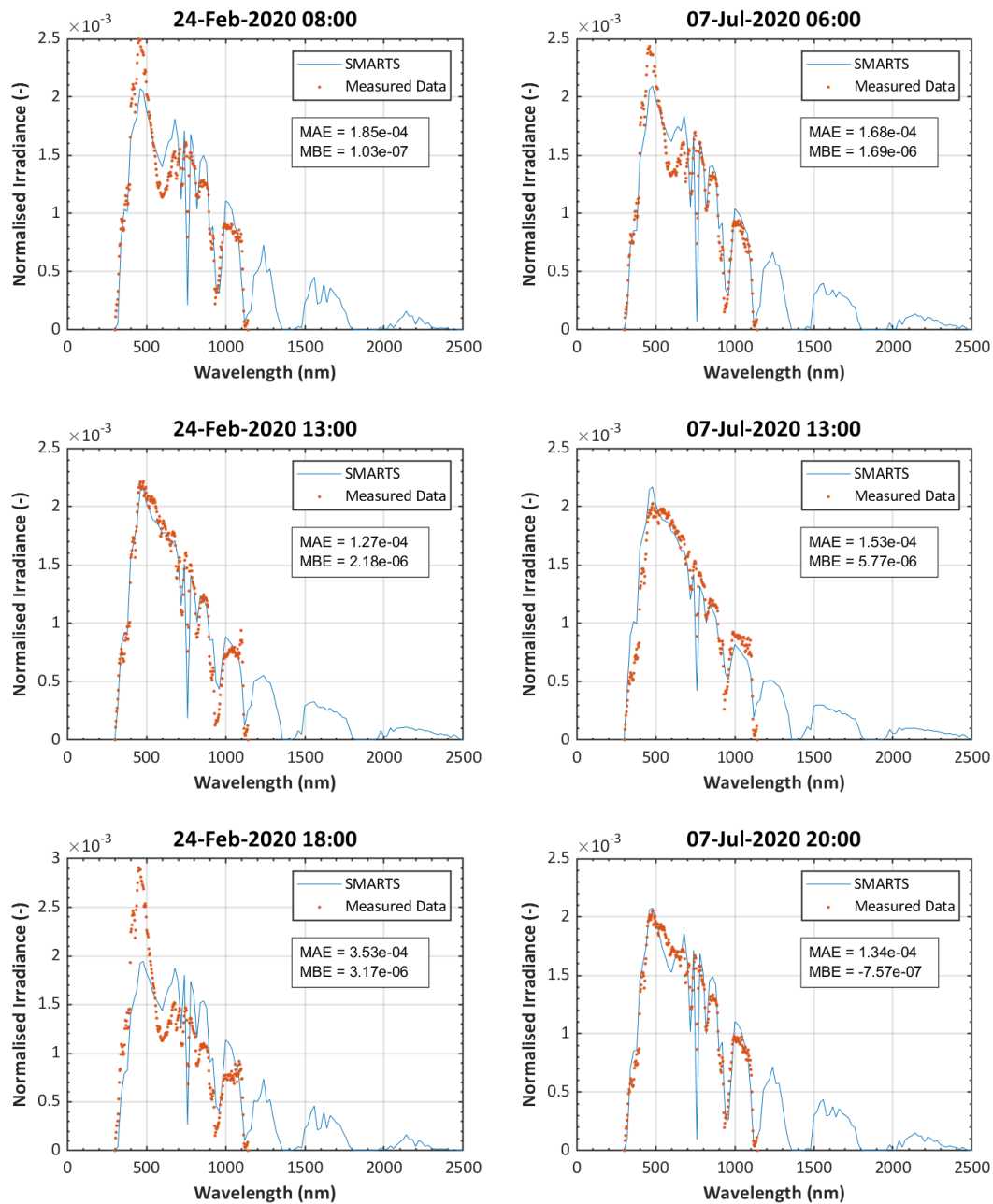


Figure 4.2: Spectral data generated by SMARTS compared to spectral measurements. The first column shows results from the 24th of February 2020, the second of the 7th of July 2020. The three rows consist of data from sunrise, highest solar point and sunset respectively.

4.4. Validating thermal model without PCM

4.4.1. System location and geometry

The combination of SMARTS and GenPro4 with the thermal model proposed in this thesis is 'compared to data from the PV monitoring station at the TU Delft. At this station three PV modules are installed (as described in the thesis by MPF Verheijen [37]) two with a PCM and one without. The model is first validated without the PCM attached. With the materials found in table 4.1 the modules are layered as follows: Glass, EVA, c-Si, copper, EVA, Tedlar, Armaflex. Armaflex is an insulating material, which is placed at the back of the modules since these modules are a prototype system for a Building Integrated PV (BIPV) + PCM system, where the backside of the modules would not be exposed to the outside air.

Material	Density ρ (kg/m ³)	Specific Heat Capacity c_p (Jkg ⁻¹ K ⁻¹)	Thermal Conductivity k (Wm ⁻¹ K ⁻¹)	Thickness (mm)	Emissivity ϵ (-)
Glass	2700	750	1.8	4	0.84
EVA	960	2090	0.32	0.45	(-)
c-Si	2300	838	149	0.18	(-)
Copper	8960	385	400	0.004	(-)
Tedlar	1370	1760	0.56	0.5	(-)
Armaflex	96	1000	0.037	19	0.8

Table 4.1: Materials used for the PV modules at the PV monitoring station of the Delft University of Technology [37].

4.4.2. Nodal network and time steps

For all simulations in this chapter the model was executed with a time step of 5 minutes. Since SMARTS only takes a thousand different solar positions per execution of the program, the time in between each weather data point is 16 minutes when simulating a whole week.

The nodal network for simulations without a PCM slab attached contains 40 nodes, divided in the following way: 4 nodes glass, 4 nodes EVA, 3 nodes silicon, one node silicon/copper, 4 nodes EVA, 4 nodes Tedlar, 20 nodes Armaflex.

The nodal network for simulations *with* a PCM slab attached (geometry specified in section 4.5.1) is divided as such: 4 nodes glass, 4 nodes EVA, 3 nodes silicon, one node silicon/copper, 4 nodes EVA, 4 nodes Tedlar, 4 nodes PET, 14 nodes PCM, 4 nodes PET, 25 nodes of Armaflex.

4.4.3. Model performance in summer

To see how the simulation performs on a high-irradiance, high-temperature day, the first week of September 2019 is used. The temperature of the PV module installed at the TU Delft, is measured with seven thermocouple between the Tedlar and Armaflex layer (of which the average measured temperature is used). For the simulation the temperature of the last node of the Tedlar layer is used for comparison. The temperatures these thermocouples measure are registered using *Picolog6.0* every ten minutes. In figure 4.3 the measured data and the simulated results are plotted together. The simulation seems to be in accordance with the measured temperatures, to get a closer look, the absolute difference between the two observations is plotted (fig 4.4).

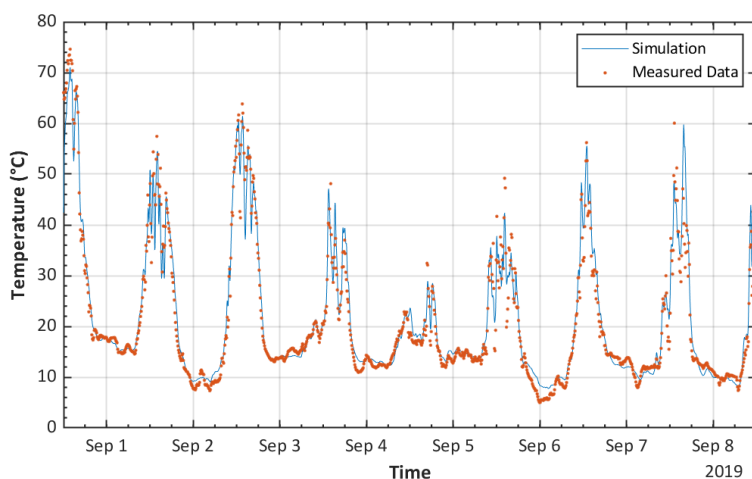


Figure 4.3: Model output and measured temperatures of a PV module during the first week of September 2019

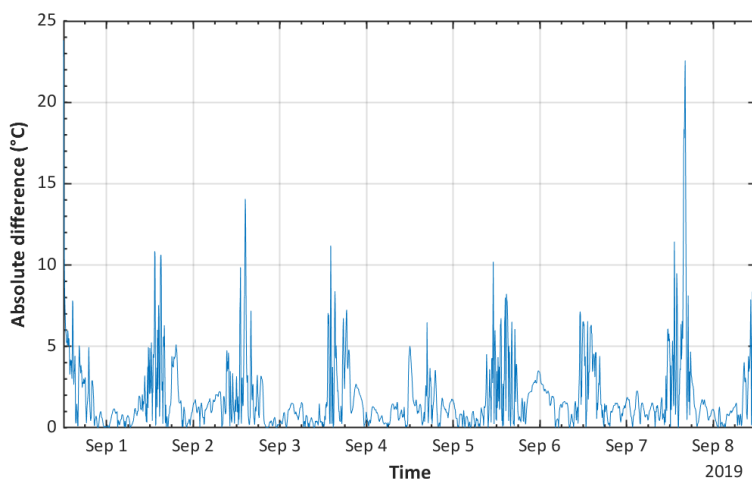


Figure 4.4: Absolute difference between the model output and the measured temperature values for a PV module, during first week of September 2019

During this first week of September 2019, the biggest difference between the measured temperature and the simulation seem to be during the day, as can be seen in figure 4.4. Yet, if the absolute difference is compared to the conventional difference (prediction minus measurement, see figure 4.5), the difference plot shows that the error is oscillating around the zero mark. This swaying around zero could be due to the fact that the simulation is calculating the correct temperatures, but just a few time steps behind or ahead, causing a higher absolute error with low bias. For a high irradiance week, and without a PCM attached, the model is working properly.

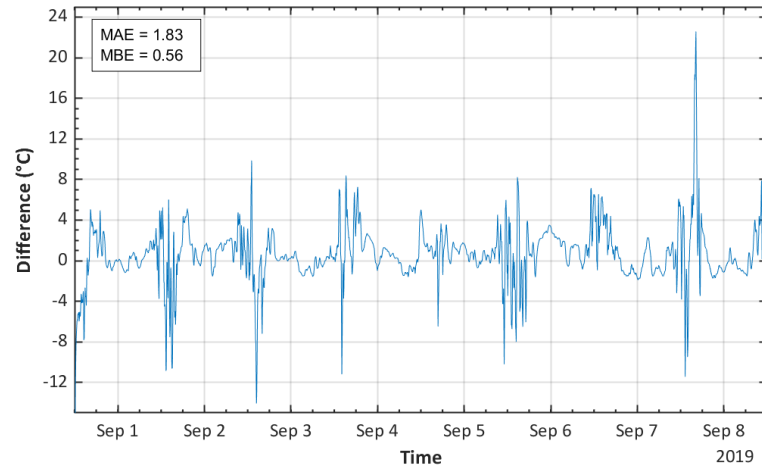


Figure 4.5: Difference (prediction - measurement) between the measured and simulated temperatures, during the first week of September 2019, of a PV module installed at the TU delft. The MAE and MBE are also shown.

4.4.4. Model performance in winter

Next up, the model is tasked to simulate a low-irradiance week, the first week of January 2020. The comparison between the simulation and measured results is shown in figure 4.6. Two main observations to be made in this comparison are the somewhat constant "offset error" and the lower simulated temperatures while the measured temperatures are peaking. The possible causes of this offset error will be discussed in more detail in chapter 5.

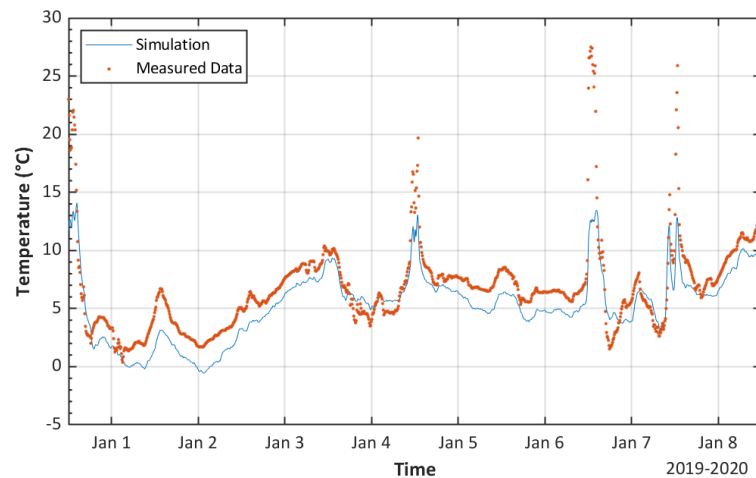


Figure 4.6: Model output and measured temperatures of a PV module during the first week of January

In figure 4.7 the absolute difference between the simulation and the measurements is plotted, in figure 4.8 regular difference (simulation minus measurement) is plotted. In both figures the offset (of around 2°C) can clearly be seen. Apart from this constant difference between the simulation and the measurement, the model seems to follow the general trends of the simulations correctly.

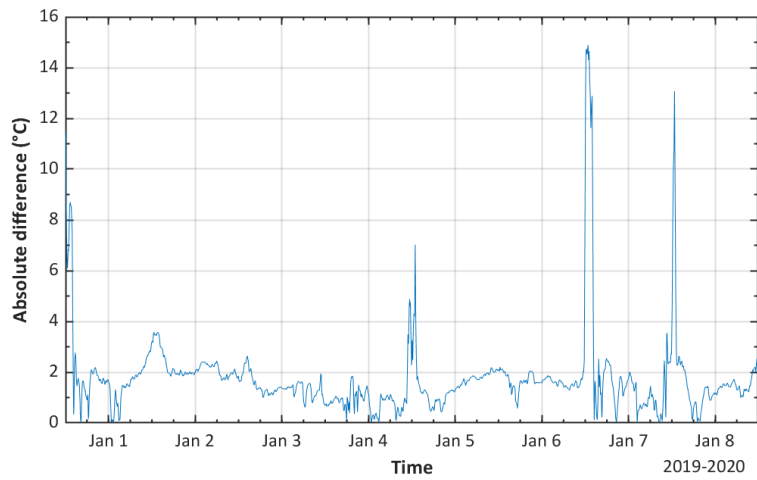


Figure 4.7: Absolute difference between the model output and the measured temperature values of a PV module, during the first week of January

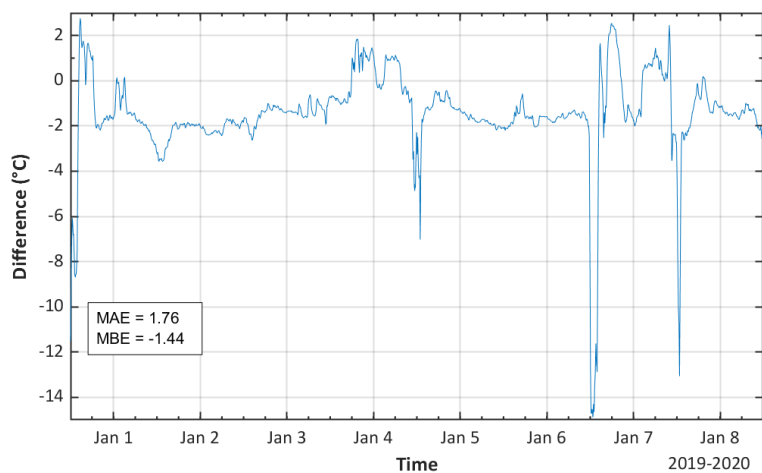


Figure 4.8: Difference (prediction - measurement) between the measured and simulated temperatures, during the first week of January 2020, of a PV module installed at the TU delft. The MAE and MBE are also shown.

4.5. PV + PCM validation

Now that the PCM model is validated separately, and the accuracy of the thermal model for a PV module is studied, they will now be combined. The temperature of an identical PV module as studied before will be simulated, but now a slab of PCM is attached to the module.

4.5.1. Physical parameters and geometry

Unfortunately the manufacturer of the PCM slabs installed at the monitoring station was not able to provide all the physical parameter inputs (such as specific heat capacity) required for the model to run properly. As an approximation of the parameters of the PCM, the values for Rubitherm-25 [38] are used. The data used for the PCM and its PET encapsulant can be found in table 4.2. One change was made to the parameters: the melting temperature was set to 23°C instead of 25°C, since it was found that the PCM installed at the monitoring station starts melting at 23°C. For the PV modules with a PCM slab attached the layer ordering becomes: Glass, EVA, c-Si, copper, EVA, Tedlar, PET, PCM, PET, Armaflex.

Material	Density ρ (kg/m ³)		Specific Heat Capacity c_p (Jkg ⁻¹ K ⁻¹)		Thermal Conductivity k (Wm ⁻¹ K ⁻¹)		Thickness (mm)
	liquid	solid	liquid	solid	liquid	solid	
PCM	750	870	1800	1800	0.2	0.2	10
PET		1380		1000		0.15	0.4

Table 4.2: Material data used for the PCM and its plastic encapsulant.

4.5.2. PV+PCM model performance during summer

The simulated results for the first week of September 2019 can be seen in figure 4.9, the simulated temperatures are higher than the measurements during the day. Figure 4.10 shows the absolute difference between the simulated and measured temperatures, figure 4.11 shows the "simulation minus measurement" difference. The errors are significantly higher and with a bigger positive bias compared to the simulations without a PCM slab. This discrepancy between the two simulations indicates a problem with the PCM model or its inputs.

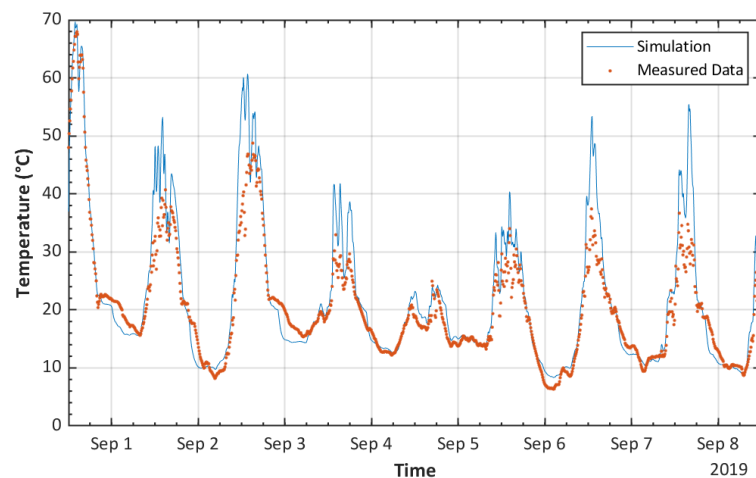


Figure 4.9: Model output and measured temperatures of the PV + PCM system in the first week of September

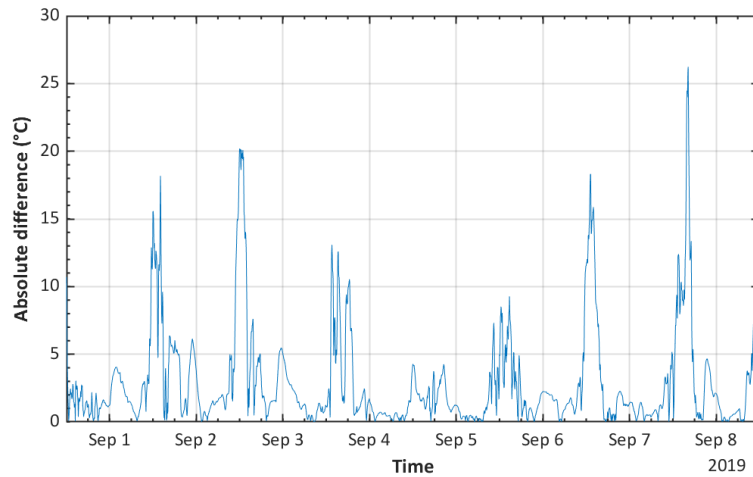


Figure 4.10: Absolute difference between the model output and the measured values of the PV + PCM system for the first week of September

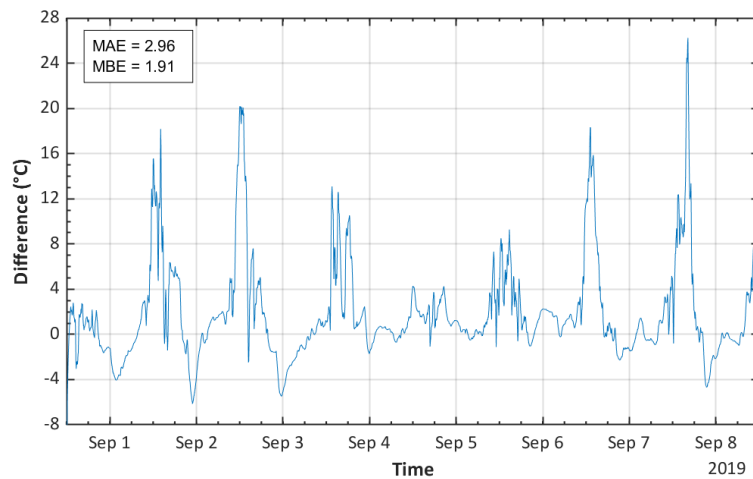


Figure 4.11: Difference (prediction - measurement) between the measured and simulated temperatures, during the first week of September 2019, of the PV + PCM system. The MAE and MBE are also shown.

4.5.3. PV+PCM model performance during winter

The module temperatures for the first week of January are also simulated for the PV + PCM system. The results can be seen in figure 4.12, both the measured data and the simulated data are very similar to their respective values in figure 4.6. The melting temperature of the PCM (23-25°C) is not reached, so no heat is being put into melting the PCM when the PV module warms up. In that sense, the PCM layer is just acts like an additional insulator.

A closer look at the differences (figures 4.13 and 4.14) shows that the shape and size of the error between measurement and simulation is very similar to that seen for the system without a PCM slab attached.

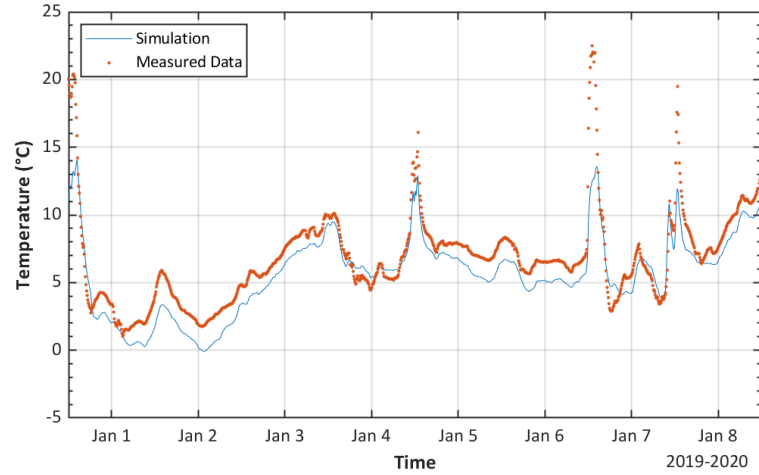


Figure 4.12: Measured and simulated module temperature of a PV + PCM system, during the first week of January 2020.

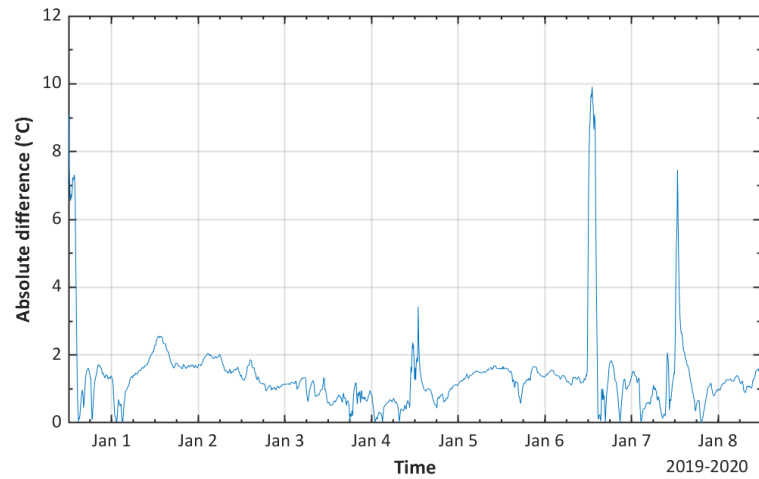


Figure 4.13: Absolute difference between simulated temperatures and measured values for the PV + PCM system, during the first week of January 2020

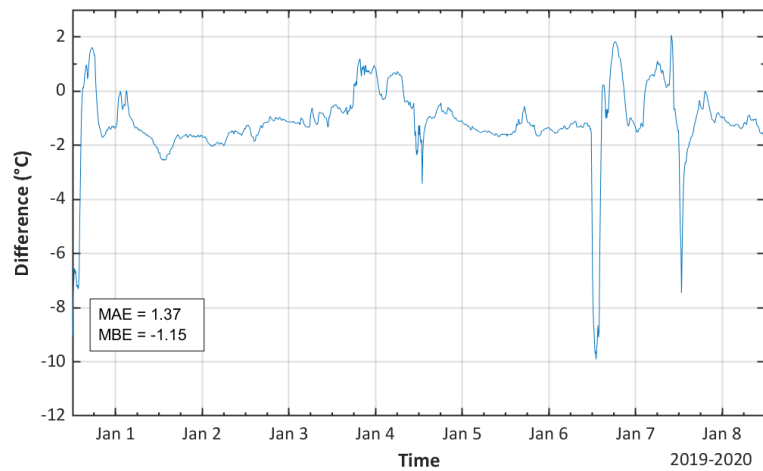


Figure 4.14: Difference (simulation - measurement) between simulated temperatures and measured values for the PV + PCM system, during the first week of January 2020. The MAE and MBE are also shown.

4.6. Review of model performance

The model has been used to simulate a summer week for a PV system with and without a PCM slab attached to the backside of the module. For a summer week without a PCM attached, the model proved to be accurate. However, when a PCM was attached the simulation temperatures were up to 20-25°C higher than measured values. Since both the thermal model and the PCM model were validated for this summer week, the issue most likely lies with the physical parameters chosen for the PCM.

The same was done for a winter week. Here the results were similar due to the melting temperature of the PCM not being reached. Both simulated results, however, had significant bias errors compared to the measured data. The possible causes for this are discussed in the following chapter.

All simulations were performed on an 4th generation ZBook mobile workstation from HP. For a simulation without PCM the model simulates 18.75 hours per real-time hour.

5

Discussion

5.1. The effects of wind speed on module temperature

The simulated temperatures during the first week of January from section 4.4.4 and 4.5.3 showed a clear bias towards lower temperatures, compared to the measurements. For the biggest part of that first week in January, the error is an offset of about 2 °C. This offset is not likely being caused by the slight spectral data mismatches seen in figure 4.2, since those would cause discrepancies near sunrise and sunset. One of the heat transfer mechanisms that is independent of the day/night cycle, yet with a strong impact on PV module temperature, is convection. This section will focus on how the way convection is calculated contribute to the presence of the aforementioned biases.

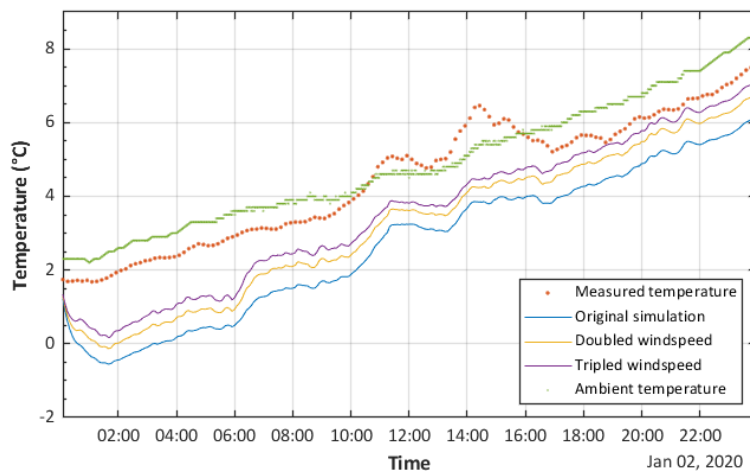


Figure 5.1: Module temperature for January 2nd 2020 for different wind speeds. The measured ambient temperature is also shown.

Figure 5.1 shows how increasing the value of wind speed affects the the outcome of the convection model (and therefore module temperature) used for the winter week in January. Increasing the wind speed causes the module temperature to rise. This might seem counter-intuitive since convection normally cools down the PV module. The increased convection warms up the module temperature because the ambient temperature is constantly rising throughout this day from 2°C at 00:01 to 8°C at 23:59 (this can also be seen in figure 5.1), while the module temperature is lower than the ambient temperature. When increasing the measured wind speeds (see figure 5.1) the simulated temperatures rise more during the end of the day compared to the beginning. In figure 5.2 the measured wind speed

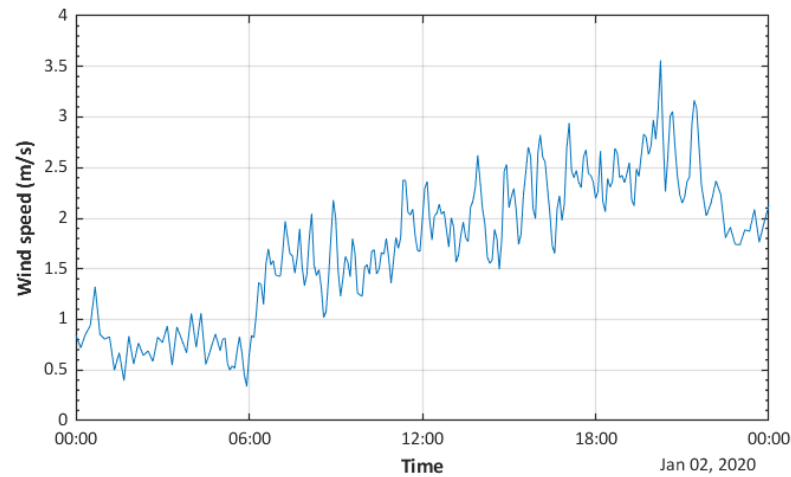


Figure 5.2: Measured wind speed at the TU Delft PV monitoring station on the 2nd of January

on the 2nd of January 2020 is shown. The lower wind speeds in the early morning cause a lower h , which causes less convective heat transfer, and thus a cooler module. The calculation of h (by Watmuff et al. [21]) used for these simulations is (eq. 2.3):

$$h = 2.8 + 3 \cdot w \quad (5.1)$$

This linear calculation of h has a rather low offset of 2.8 compared to other linear h models [20]. To analyse the effect of a different h calculation the module temperature is simulated for the same day in January (figure 5.3), but this time with the following calculation for h , by Test et al. [39]:

$$h = 8.55 + 2.56 \cdot w \quad (5.2)$$

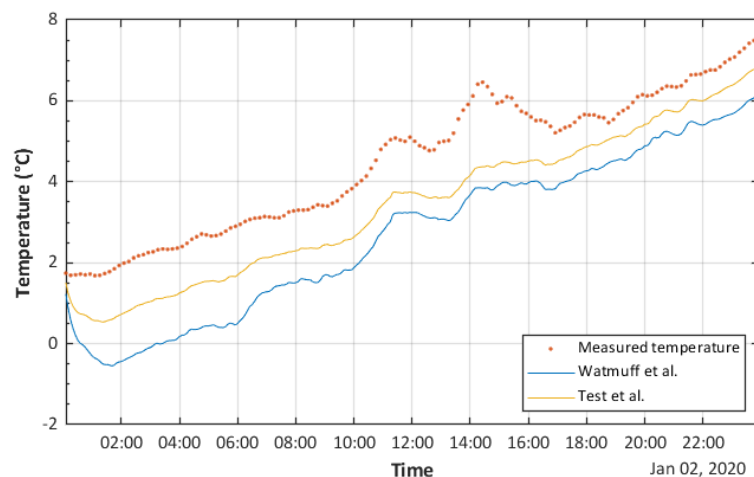


Figure 5.3: Module temperature for January 2nd 2020 for different convection heat transfer coefficient calculations. The baseline uses equation 5.1, the higher offset refers to equation 5.2.

Figure 5.3 shows that the use of this model more evenly increases the module temperature over the course of the day. To see the impact on accuracy, this model is used to simulate the full first week of January, in order to compare it to the results from chapter 4 (see figure 5.4). To get a closer view off the differences between the measurements and the simulated temperatures, the difference and absolute

difference are shown again (figures 5.5 and 5.6) together with the Mean Absolute Error (MAE) and Mean Bias Error (MBE).

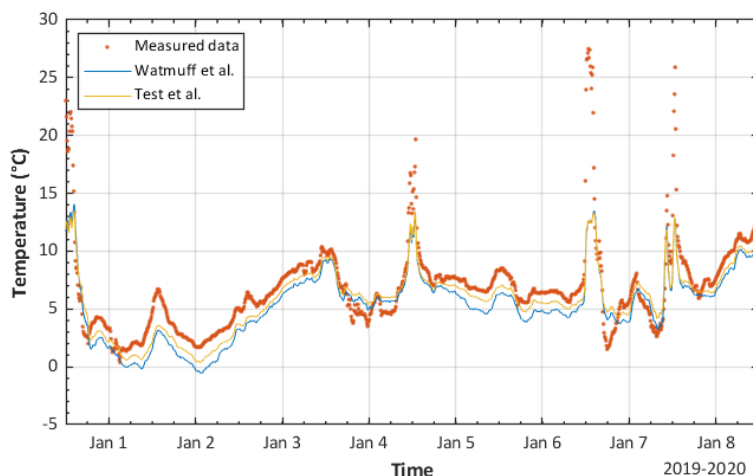


Figure 5.4: Measured and simulated module temperatures for the first week of January 2020. The different h models refer to eq. 5.2 and eq. 5.2

Comparing figure 5.6 and 4.8 the MAE has decreased from 1.76 to 1.39 and the MBE from -1.44 to -0.92. Especially the MBE improved due to changes in the h -model as expected, since h is now higher for every wind speed, due to the higher offset value in the calculation. This section has shown that the choice of convection model is very influential to the simulated module temperature. In this particular case the chosen convection model (eq 5.2) was not the best choice yet, since the simulated temperatures were still about a centigrade too low. For future work it is therefore recommended to thoroughly research the convection model required when using the model presented in this thesis.

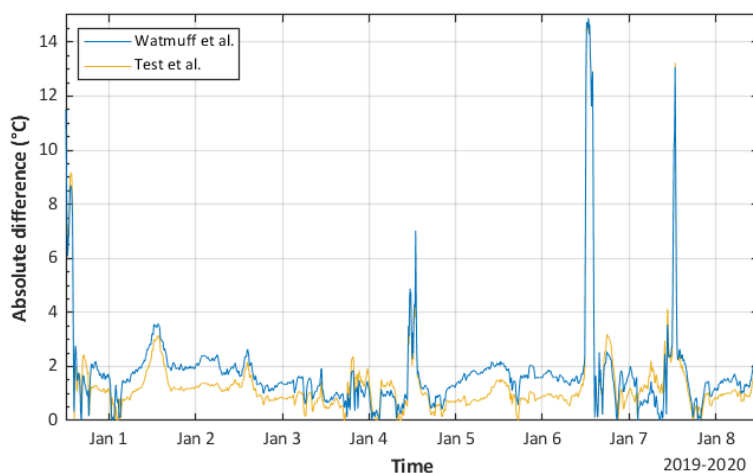


Figure 5.5: Absolute difference between measurements and the simulated module temperatures shown in figure 5.4.

5.2. Sensitivity analysis on PCM parameters

In chapter 4 the PCM model was validated separately and the module temperatures during a week in summer were simulated properly without a PCM attached. Yet when combined the model did not perform properly. The thermophysical parameters used for the PCM were those of Rubitherm-25, which is different to the PCM actually installed at the back of the measured PV modules. In order to find out

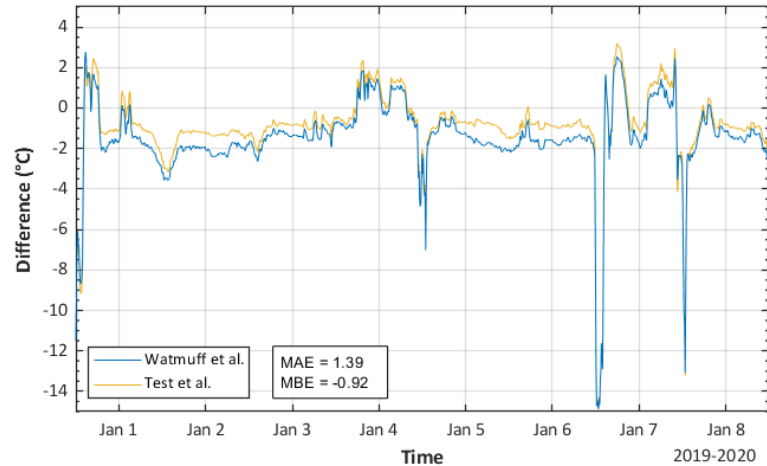


Figure 5.6: Difference (prediction - observation) between measurements and the simulated module temperatures shown in figure 5.4. The MAE and MBE refer to the error between the measured temperatures and the simulated temperatures using Test et al.

what the actual parameters are, a sensitivity analysis should be performed. A sensitivity analysis for the thermophysical parameters of a PCM is complex however, since there are many parameters: thickness, latent heat of fusion, density (both liquid and solid), specific heat capacity (both liquid and solid) and thermal conductivity (both liquid and solid). In order to reduce the amount of parameters, the analysis will focus on the thermal diffusivity, α (calculated as $\alpha = \frac{k}{\rho c_p}$). The α for Rubitherm-25 is approximately $1.2 \cdot 10^{-7} \text{m}^2/\text{s}$ (see table 4.2).

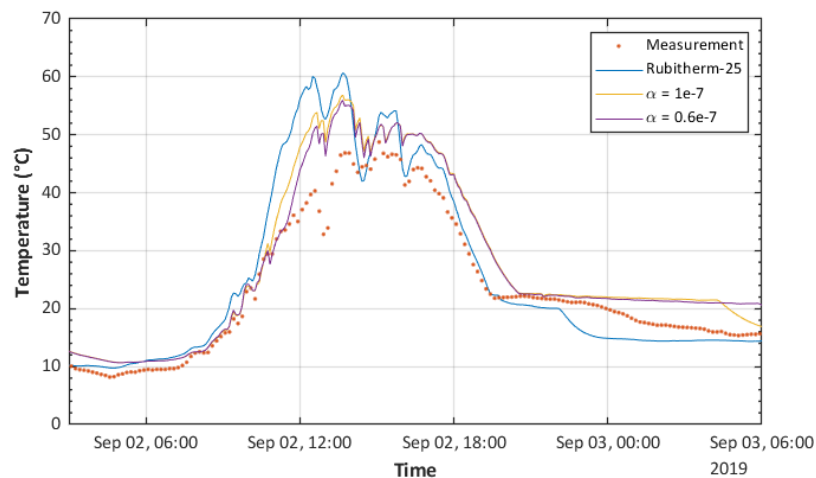


Figure 5.7: measured and simulated PV module temperatures for the second day of September 2019. The module temperatures are simulated for different thermal diffusivities (α) and compared with the original simulation (Rubitherm-25)

In figure 5.7 the measured module temperature and the previously simulated temperature with Rubitherm-25 data for September 2nd are shown. In addition a simulation is run with both the solid and liquid α set to $1.0 \cdot 10^{-7} \text{m}^2/\text{s}$, by making $c_p = 2500 \text{J/kgK}$, $\rho = 2000 \text{kg/m}^3$ and $k = 0.5 \text{W/mK}$, which are closer to the values used by Verheijen [37]. The effect of decreasing the thermal diffusivity, α , from $1.2 \cdot 10^{-7} \text{m}^2/\text{s}$ to $1.0 \cdot 10^{-7} \text{m}^2/\text{s}$ can be seen in the slower rise and fall in temperature. The changes to the thermophysical parameters also caused the 'plateauing' that can be seen at the end of the day to be elongated. To show this effect more clearly the k value is changed to 0.3, resulting in a α of $0.6 \cdot 10^{-7} \text{m}^2/\text{s}$. The results in figure 5.7 show how decreasing the thermal diffusivity increases the time the PCM takes to solidify, creating an longer plateau in temperature.

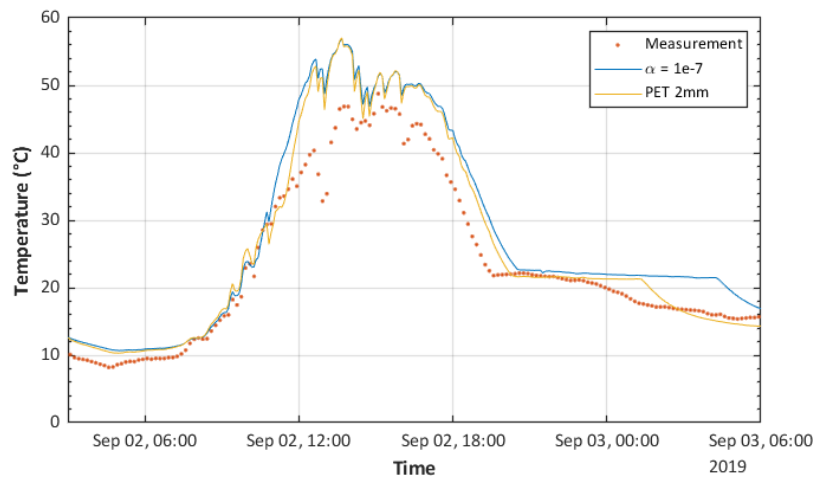


Figure 5.8: measured and simulated PV module temperatures for the second day of September 2019. The module temperatures are simulated with a different thickness distribution in the PCM slab.

Apart from differences in α and its related parameters, the difference between Rubitherm-25 and the PCM used in the monitored PV modules could also lay in the latent heat of fusion or the thickness of the PCM. Only the thickness of the PCM plus its encapsulant is known, so the PCM could be thicker or thinner than assumed. The PCM could also be under-performing compared to its data sheet, not being able to store as much heat as advertised, due to degradation [40].

In figure 5.8, the module temperature is simulated with the same $\alpha = 1 \cdot 10^{-7} \text{m}^2/\text{s}$ as mentioned before, but also with a thicker PET encapsulant. The PET thickness is increased from 0.4mm to 2mm, decreasing the PCM thickness from 10 to 6.8 mm (since the total thickness is known). Changing the thicknesses of the PCM slab has led to a small decrease in temperature across the day, and a shortening of the plateau.

This section has shown that many factors shape the way the PCM melts and conducts heat. Finding where the installed PCM differs from Rubitherm-25 is a difficult task since all the parameters influence each other. The process of finding the right parameters is encumbered even more due to uncertainties in thickness and PCM degradation.

6

Conclusions and Outlook

6.1. Conclusion

This thesis has provided a model that can aid in the research of thermal management for PV modules, with a focus on the use of PCMs. The model is flexible, spectrally resolved and able to visualise the temperature profile of a PV module while it is warming up or cooling down.

By using SMARTS to generate spectral data, the model can use spectral data without the need for spectral measurements, leaving only external parameters that are easier to obtain: irradiance, ambient temperature and wind speed. The model also requires location specific inputs, such as geographic coordinates, module elevation and module tilt.

Another factor that expands the usability of this model, is the use of GenPro4. This software package calculates the absorption of light in each layer of a PV cell, it supports almost any type of PV cell arrangement (e.g. anti-reflective coatings, layer texturing, bi-facial PV cells). This is why using GenPro4 adds flexibility to the model.

By combining irradiance data, SMARTS and GenPro4 the model is able to calculate how much heat is absorbed in each layer of the PV cell. By using a transient thermal model with fine meshing, the model is able to show how this absorbed heat moves through the module. In doing so it visualizes and aids future work in understanding the heat transfer processes at play when a PV module is warming up or cooling down.

The thermal model is expanded upon by being able to add a PCM layer to the module. As mentioned before, PCMs have great potential in the cooling of PV modules. This model is able to show how quickly the PCM layer changes phase as the PV module heats up or cools down.

6.2. Model improvements

6.2.1. Improving computational times

As mentioned in section 4.6, the model can currently simulate 45 hours of data per hour for a time step of 5 minutes, without a PCM and 18.75 hours per hour with a PCM. Since the model uses several external packages (SMARTS, SPA and GenPro4) and uses the algorithm by Zivkovic for the PCM, the main place to increase the speed of the model is in solving the matrix equations. Currently this is done with the Gauss-Siedel method, which is reliable but rather slow since it needs to iterate several times. Due to the use of this rather simple solving algorithm the model only uses a fraction of a typical commercial laptop's CPU capacity. This could be seen as an indication for improvement, using an algorithm that can more effectively use the resources of the PC (like a Krylov subspace method [41] or other forms of parallelisation [42]).

6.2.2. Adding electrical output

In the current state of the model, the temperature coefficient on the data sheet of the PV cell is used to determine how much of the incoming irradiance is converted into electrical energy. Adding a more robust electrical model would be a big step forward for the model. The work in progress by Andres Calcabrini [43] could possibly be used for this purpose. Calcabrini's model gives, among other outputs, the V_{oc} and I_{sc} at different operating temperatures of any typical c-Si solar cell.

6.2.3. Improving SMARTS integration

In section 4.4.2 it's mentioned how SMARTS can take a 1000 solar position data points per execution of the program. For now, the model makes sure that this limit is not exceeded. This could be improved upon by making the model run SMARTS multiple times based on the amount of solar position inputs specified by the user.

6.2.4. Adding cloudiness dependency to spectral irradiance data

In chapter 4 the results from SMARTS are compared to measured spectral data. Especially on the low-irradiance day in January SMARTS differed from the measurements. This could be due to the fact that SMARTS is to simulate spectra for clear days. If the model were able to adjust the spectra created by SMARTS to resemble the solar spectrum on a cloudy day this could improve the model's performance. This would also, however, require some sort of knowledge about the cloudiness on a specific day (this can either be measured or predicted [44]).

6.2.5. Improving physical inputs

For the validation simulations in chapter 4, the physical parameters of Rubitherm-25 were used, not values from the PCM that was actually installed. The model accuracy would benefit from having more accurate data of the PCM and its casing. The main use for the PCM slabs installed at the PV monitoring station is heat insulation for buildings. For use in buildings, the most important parameter is how much energy can be stored at what temperatures. When modelling the PCM, more parameters are required however: the specific heat capacity for both the liquid and solid phase, density for both phases and thermal conductivity for both phases. The exact material and thickness of the plastic casing around the PCM are also unknown. The analysis in section 5.2 showed that the PCM parameters are all related to each other, making it difficult to determine which parameters need to be changed in order to more accurately represent the PCM used for the validation simulations.

6.3. Model applications

6.3.1. Mapping the global potential of PV + PCM systems

Since the model only requires irradiance, ambient temperature and wind speed as weather data, the model can easily run simulations for places all over the globe. This could be useful for finding the areas of the world that would benefit most from adding PCMs to PV systems. Because of the flexibility of the model, this could be done for all kinds of configurations: from standalone modules, to building integrated PV.

6.3.2. Integration with the PV systems modelling toolbox of the PVMD group

An ongoing project within the Photovoltaic Materials and Devices (PVMD) group at the Delft University of Technology is the creation of a comprehensive PV systems modelling toolbox. The model presented in this thesis could possibly be adapted to fit the requirements of the toolbox' framework, giving users access to more detailed thermal simulations and the possible addition of PCMs to their simulated PV modules.

Bibliography

- [1] Hannah Ritchie. Renewable energy. *Our World in Data*, 2017. <https://ourworldindata.org/renewable-energy>.
- [2] ISE. Photovoltaics report, 9 2020. URL <https://www.ise.fraunhofer.de/content/dam/ise/de/documents/publications/studies/Photovoltaics-Report.pdf>.
- [3] Armin Richter, Martin Hermle, and Stephan W. Glunz. Reassessment of the limiting efficiency for crystalline silicon solar cells. *IEEE Journal of Photovoltaics*, 3:1184–1191, 2013.
- [4] NREL. Best research-cell efficiency chart. URL <https://www.nrel.gov/pv/cell-efficiency.html>.
- [5] Hossein Mousazadeh, Alireza Keyhani, Arzhang Javadi, Hossein Mobli, Karen Abrinia, and Ahmad Sharifi. A review of principle and sun-tracking methods for maximising solar systems output. *Renewable and Sustainable Energy Reviews*, 13:1800–1818, 2009.
- [6] Robert McConell. Concentrator photovoltaic technologies: Review and market prospects. *Refocus*, 6:35–39.
- [7] Natarjan Shanmugan, Rishi Pugazhendhi, Rajvikram M. Elavarasan, Pitchandi Kasiviswanathan, and Narottam Das. Anti-reflective coating materials: A holistic review from pv perspective. *Energies*, 13, 2020.
- [8] Leonard Forbes. Texturing, reflectivity, diffuse scattering and light trapping in silicon solar cells. *Solar Energy*, 86:319–325, 2012.
- [9] P. Mandal and S. Sharma. Progress in plasmonic solar cell efficiency improvement: A status review. *Renewable and Sustainable Energy Reviews*, 65:537–552, 2016.
- [10] Emmanuel Van Kerschaver. Back-contact solar cells: a review. *Progress in Photovoltaics*, 14: 107–123, 2005.
- [11] Osarumen O. Ogbomo, Emeka H. Amalu, N.N. Ekere, and P.O. Olagbegi. Effect of operating temperature on degradation of solder joints in crystalline silicon photovoltaic modules for improved reliability in hot climates. *Solar Energy*, 170:682–693, 2018.
- [12] MATLAB. *version 9.6.0.1174912 (R2019a) Update 5*. The MathWorks Inc., Natick, Massachusetts, 2020.
- [13] The sun's energy. URL <https://ag.tennessee.edu/solar/Pages/What%20Is%20Solar%20Energy/Sun%27s%20Energy.aspx>.
- [14] Cutler J. Cleveland and Christopher Morris, editors. *Handbook of Energy*, volume 1. Elsevier, 2013. ISBN 978-0-08-046405-3. doi: <https://doi.org/10.1016/C2009-0-16729-6>.
- [15] Physics labs for scientists and engineers: Electricity & magnetism, 2012.
- [16] *Inorganic Chemistry*. LibreTexts, 2019.
- [17] Tatsuo Saga. Advances in crystalline silicon solar cell technology for industrial mass production. *NPG Asia materials*, 2:96–102, 2010.
- [18] URL <https://www.benning.de/products-en/testing-measuring-and-safety-equipment/measuring-devices-for-photovoltaic/pv-2/faq.html>.

- [19] Frank P. Incropera, David P. DeWitt, Theodore L. Bergman, and Adrienne S. Lavine. *Fundamentals of Heat and Mass Transfer Sixth Edition*. Wiley, 2007.
- [20] J.A. Palyvos. A survey of wind convection coefficient correlations for building envelope energy systems' modeling. *Applied Thermal Engineering*, 28:801–808, 2008.
- [21] J.H. Watmuff, W.W.S. Charters, and D. Proctor. Solar and wind induced external coefficients for solar collectors. *Comptes. Int. Rev. d'Hellio Tech*, 1977.
- [22] Daisuke Sato and Noboru Yamada. Review of photovoltaic module cooling methods and performance evaluation of the radiative cooling method. *Renewable and Sustainable Energy Reviews*, 104:151–166, 2019.
- [23] S. Sargunanathan, A. Elango, and S. Tharves Mohideen. Performance enhancement of solar photovoltaic cells using effective cooling methods: a review. *Renewable and Sustainable Energy Reviews*, 64:382–393, October 2016.
- [24] Juan C. Ortiz Lizcano. Thermal management of pv modules: Passive cooling solutions for front and back surfaces, 2019.
- [25] J.C. Ortiz Lizcano, G. Frantzi, G. Yang, H. Ziar, M. Zeman, and O. Isabella. Complete performance model for optimal coloured photovoltaic module design based on optic filters for building integrated applications. 2020.
- [26] Tao Ma, Zhenpeng Li, and Jiaxin Zhao. Photovoltaic panel integrated with phase change materials (pv-pcm): technology overview and materials selection. *Renewable and Sustainable Energy Reviews*, 116, 2019.
- [27] H. Mahamudul, M. Rahman, H. Metselaar, S. Mekhilef, S. Shezan, R. Sohel, and et al. Temperature regulation of photovoltaic module using phase change materials: a numerical analysis and experimental investigation. *Int J Photoenergy*, 2016.
- [28] R. Thaib, T. Mahlia, and N.A. Pambudi. Experimental analysis of using beeswax as phase change materials for limiting temperature rise in building integrated photovoltaics. *Case studies in Thermal Engineering*, 12:223–227, 2018.
- [29] Jacob Maxa, Andrej Novikov, and Mathias Nowotnick. Thermal peak management using organic phase change materials for latent heat storage in electronic applications. *Materials*, 11, December 2018. doi: 10.3390/ma11010031.
- [30] I. Reda and A. Andreas. Solar position algorithm for solar radiation applications. *Solar Energy*, 76:577–589, 2004.
- [31] Christian A. Gueymard. *SMARTS code, version 2.9.5 For Windows User's Manual*, December 2005.
- [32] R. Santbergen, T. Menguro, T. Suezaki, G. Koizumi, K. Yamamoto, and M. Zeman. Genpro4 optical model for solar cell simulation and its application to multijunction solar cells. *IEEE Journal of Photovoltaics*, 7:919–926, 2017.
- [33] B. Zivkovic. An analysis of isothermal phase change of phase change material within rectangular and cylindrical containcers. *Solar Energy*, 70(1):51–61, 2001.
- [34] Müslüm Arici, Feyza Bilgin, Sandro Nizetic, and Agis M. Papadopoulos. Phase change material based cooling of photovoltaic panel: A simplified numerical model for the optimization of the phase change material layer and general economic evaluation. *Journal of Cleaner Production*, 189:738–745, 2018.
- [35] V.R. Voller. Fast implicit finite-difference method for the analysis of phase change problems. *Numerical Heat Transfer*, 17:155–169, 1990.
- [36] A. D. Solomon. An easily computable solution to a two-phase stefan problem. *Solar Energy*, 23: 525–528, 1979.

-
- [37] M.P.F. Verheijen. Thermal management of photovoltaics using phase change materials. Master's thesis, Delft University of Technology, 2019.
- [38] Rubitherm. Rt25hc datasheet, 1 2020.
- [39] F.L. Test, R.C. Lessmann, and A. Johary. Heat transfer during wind flow over rectangular bodies in the natural environment. *Trans. ASME J. Heat Transfer*, 103:262–267, 1981.
- [40] Navin Kumar, Jason Hirschey, Tim J. Clair, Kyle R. Gluesenkamp, and Samuel Graham. Review of stability and thermal conductivity enhancements for salt hydrates. *Journal of Energy Storage*, 24, 2019.
- [41] Y. Saad. *Iterative Methods for Sparse Linear Systems*. Society for Industrial and Applied Mathematics, 2003.
- [42] Parallel dense gauss-siedel algorithm on many-core processors. 2009.
- [43] A. Calcabrini, R. Weegink, M. Zeman, and O. Isabella. Reconfigurable modules for higher yields in urban pv systems - a simulation study. 2020.
- [44] H.N. Singh and G.N. Tiwari. Evaluation of cloudiness/haziness factor for composite climate. *Energy*, 30:1589–1601, 2005.